



**POLITECNICO**  
**MILANO 1863**

# Preliminary design of a reusable airborne launcher

*Project Group **TERR-1***

Authors	Personal Code
Bianco Samuele	10733366
Campanino Mattia	10939529
Cutino Sveva	11002455
D'Annunzio Valentina	10729511
D'Antonio Antonio	10992749
Dell'Aera Nicola	10987097
de Pinto Alessio	11012259
Orsenigo Samuele	10835389
Santoro Emanuele	10668183
Varli Arda	10976684

Prof. Filippo Maggi and Prof. Stefania Carlotti  
Academic Year 2024-2025

## Abstract

This study presents the preliminary conceptual design of a reusable airborne launch system, TERR-1, capable of delivering up to 250 kg of payload to a low Earth Sun-Synchronous Orbit. Focused on a single design iteration, this analysis serves as an initial framework to evaluate feasibility and identify areas for refinement. The design process begins by defining the high level requirements derived from customer needs, selecting LauncherOne, Electron, and Falcon 9 as baselines. The mission analysis subsystem sets the  $\Delta v$  budget. The propulsion subsystem relies on off-the-shelf Rutherford engines utilizing low-toxicity RP-1/LOX propellant. Aerodynamic analyses optimize lift and drag coefficients across subsonic to supersonic flight conditions while ensuring stability. Complementing this, the trajectory design focuses on achieving the target orbit through optimized ascent and includes a vertical re-entry strategy for the first stage to ensure reusability. Structural design integrates mass estimation relationships with stress analysis to determine thickness requirements and validate resilience. The feasibility of employing the Boeing 747-400 as a carrier is examined as well. To ensure robustness, Monte Carlo simulations assess design stability, while cost analyses evaluate Return On Investment by factoring in manufacturing, operations, and recovery costs. This preliminary analysis lays the groundwork for future iterations, facilitating a systematic approach to develop a competitive and sustainable airborne launch system.



# Contents

<b>1 Requirements and Functional Decomposition</b>	<b>1</b>
1.1 Definition of Requirements . . . . .	1
1.2 Functional decomposition . . . . .	1
1.3 Baseline Selection . . . . .	2
<b>2 Mission Analysis</b>	<b>2</b>
<b>3 Propulsion System</b>	<b>3</b>
3.1 Propellant Couple selection . . . . .	3
3.2 Engine Selection . . . . .	3
<b>4 Masses</b>	<b>4</b>
4.1 Preliminary Dimensioning . . . . .	4
4.2 Masses model . . . . .	5
4.2.1 Staging process . . . . .	5
4.2.2 Staging optimization . . . . .	6
4.2.3 MERs & Thickness computation . . . . .	7
4.3 Staging results . . . . .	8
4.4 MERs & thickness results . . . . .	8
<b>5 Aerodynamics</b>	<b>9</b>
5.1 Jørgensen-Allen approach . . . . .	9
5.2 Panel Model Central body approach . . . . .	9
5.2.1 Modified Newton method . . . . .	10
5.2.2 Krasnov Equation . . . . .	10
5.2.3 Supersonic method for slender bodies . . . . .	10
5.2.4 Fin panel method . . . . .	11
5.2.5 Aerodynamic results . . . . .	11
<b>6 Trajectory</b>	<b>12</b>
6.1 Introduction . . . . .	12
6.2 Ascent phase . . . . .	12
6.2.1 Evasive maneuver . . . . .	13
6.2.2 Modeling approach . . . . .	13
6.2.3 Optimized Trajectory results . . . . .	15
6.3 Re-entry of First stage . . . . .	18
6.3.1 Thermal Analysis of Hypersonic Retro-propulsion for Reusable Launch Vehicles	19
6.3.2 Re-entry and Landing hardware . . . . .	20
6.3.3 Re-entry Trajectory Simulation . . . . .	20
6.4 Re-entry of second stage . . . . .	22
<b>7 Structures</b>	<b>23</b>
7.1 Discretization of Launcher . . . . .	23
7.2 Internal Loads and Stresses . . . . .	24
7.2.1 Axial Forces, Shear and Bending Moment . . . . .	24
7.3 Final Structure . . . . .	25
7.4 Boeing 747-400 structural verification . . . . .	25
<b>8 Monte Carlo Analysis</b>	<b>26</b>
<b>9 Costs analysis and Return On Investment (ROI)</b>	<b>27</b>
<b>10 Conclusions and Future Improvements</b>	<b>28</b>

<b>A Appendix A: House of Quality</b>	<b>I</b>
<b>B Appendix B: Propulsion</b>	<b>II</b>
<b>C Appendix C: Masses and Structures</b>	<b>III</b>
C.1 Matrix of reaction forces . . . . .	III
C.2 Mechanical stresses . . . . .	III
<b>D Appendix D:Aerodynamics</b>	<b>V</b>
D.1 Barrowman equation . . . . .	V
<b>E Appendix E: Trajectory</b>	<b>VI</b>
E.1 Evasive maneuver equations . . . . .	VI
E.2 Ascent trajectory equations . . . . .	VI
E.3 First stage re-entry . . . . .	VI
E.4 Second stage re-entry . . . . .	IX
E.5 SSO Orbit . . . . .	X
E.6 Equatorial Orbit . . . . .	XII
<b>F Appendix F: Monte Carlo Analysis</b>	<b>XV</b>
<b>G Appendix G: Costs analysis and Return On Investment (ROI)</b>	<b>XVI</b>

## Nomenclature

$\Delta v_{ascent}$	Delta velocity provided during the ascent phase
$\Delta v_{i,landing}$	Delta velocity needed for re-entry of the i-th stage
$\Delta v_{tot}$	Total delta velocity provided by the launcher
$\dot{\gamma}$	Derivative of flight path angle
$\dot{m}$	Mass flow rate
$\dot{q}$	Heat flux
$\epsilon$	Nozzle expansion ratio
$\epsilon_i$	Structural mass index of the i-th stage
$\epsilon_{i,landing}$	Re-entry structural mass index of the i-th stage
$\eta$	Specific impulse efficiency
$\gamma$	Flight path angle
$\gamma_f$	Target flight path angle
$\omega$	Angular Position of the radius vector in 2D model
$\phi$	Carrier bank angle
$\rho$	Atmosphere density
$\rho_r$	Reference density
$\rho_{prop}$	Propellant density
$\theta$	Carrier pitch angle
$\theta_{i,j}$	Local incidence angle of i-th, j-th panel
$A$	Cross-sectional area
$A_{ref}$	Cross section area
$A_{wet}$	Wet area
$b$	Wing span
$C_a$	Axial coefficient
$C_D$	Drag coefficient
$C_L$	Lift coefficient
$C_n$	Normal coefficient
$C_p$	Pressure coefficient
$C_{pi,j}$	Pressure coefficient for i-th, j-th panel
$C_R$	Fin root chord
$C_T$	Fin tip chord

$c_i$	Characteristic exhaust velocity of the i-th stage
$C_{p,Kri,j}$	Krasnov pressure coefficient of i-th, j-th panel
$C_{p,max}$	Max pressure coefficient
$CFD$	Computational Fluid-Dynamics
$CpF$	Cost per Flight
$D$	Drag
$d$	Diameter of the nose
$d_F$	Diameter at front of transition
$D_i$	Diameter of the i-th stage
$d_R$	Diameter at rear of transition
$D_t$	Nozzle throat diameter
$D_{e1}$	Nozzle exit diameter of the first stage engines
$D_{e2}$	Nozzle exit diameter of the second stage engines
$E$	Young's Modulus
$ELV$	Expendable launch vehicle
$EM$	Expendable mass
$F_{axial}$	Axial force
$F_{shear}$	Shear force
$g_0$	Earth gravitational acceleration
$GLOM$	Gross lift off mass
$h_{dome}$	Height of the tank dome
$h_n$	Height of $n^{th}$ component
$HoQ$	House of quality
$I$	Area moment of inertia
$I_{sp,i}$	Specific impulse of the i-th stage
$I_{spid,opt}$	Ideal specific impulse in optimal conditions
$I_{spid,vac}$	Ideal vacuum specific impulse
$I_{spopt,re}$	Real specific impulse in optimal conditions
$I_{spvac}$	Vacuum specific impulse
$k$	Specific heat ratio
$L$	Lift
$L_F$	Length of fin mid chord line
$L_N$	Nose length

$L_T$	Length of transition
$L_{max}$	Lift at maximum load factor on semi-wing
$L_{tot}$	Length of the launcher
$LV$	Launch Vehicle
$Le_i$	Length of the i-th stage
$M$	Mach number
$M_\infty$	Relative Mach
$M_S$	Structural mass
$M_{0,i}$	Mass of the i-th stack before ignition
$M_{bending}$	Bending moment
$M_{f,i}$	Mass of the i-th stack after burn-out
$M_{fu}$	Airplane fuel mass
$M_{mol}$	Molar mass
$M_{P,i}$	Total propellant mass of the i-th stage
$M_{pay,i}$	Payload mass of the i-th stage
$M_{Pi,ascent}$	Propellant mass allocated for the ascent of the i-th stage
$M_{Pi,landing}$	Propellant mass allocated for re-entry of the i-th stage
$M_{S,1,staging}$	Structural mass of the i-th stage computed with the staging method
$M_{S,i,MER\&t}$	Structural mass of the i-th stage computed with the MERs&t method
$M_{S,i}$	Structural mass of the i-th stage
$MTOW$	Max take-off weight
$N$	Number of fins
$n_i$	Inverse of the mass ratio
$n_{max}$	Max load factor
$n_x$	$x^{th}$ loading factor
$P_0$	Local total pressure
$P_0$	Sea-level atmospheric pressure
$P_\infty$	Reference pressure
$P_c$	Chamber pressure
$P_e$	Exhaust pressure
$P_i$	Percentage of total propellant allocated for re-entry of the i-th stage
$P_s$	Initial total pressure
$P_{atm,h}$	Atmospheric pressure at the specific height

$p_h$	Tank pressure
$q$	Dynamic pressure
$R$	LV radius
$r$	Norm of the position vector
$R_0$	Universal gas constant
$R_\oplus$	Earth radius
$RLV$	Reusable launch vehicle
$ROI$	Return on Investment
$S$	Fin semispan
$SAS$	Stability Augmentation System
$SM$	Aerodynamic stability margin
$T$	Thrust
$t$	Thickness
$T_0$	Sea-level temperature
$t_{b,ascent}$	Burning time for the ascent phase
$t_{b,landing}$	Burning time for the re-entry phase
$t_{b1}$	First stage burning time
$t_{b2}$	Second stage burning time
$T_{grad}$	Temperature lapse rate
$T_{height}$	Temperature at the specific height
$TPS$	Thermal Protection System
$TVC$	Thrust Vector Control
$v_\infty$	Reference velocity
$v_f$	Target velocity
$v_0$	Initial velocity of the launcher
$v_{carrier}$	Velocity of the carrier
$v_{Earth}$	Radial velocity of the Earth
$X_B$	Distance from nose tip to fin root chord leading edge
$X_P$	Distance from tip nose to front of transition
$X_R$	Distance between fin root and fin tip leading edges
$z$	Altitude
$z_f$	Target altitude

## List of Figures

1	Functional decomposition . . . . .	2
2	Cluster configuration . . . . .	4
3	Payload dimensions estimation . . . . .	5
4	3-D Launcher model . . . . .	9
5	Local cone approximation <sup>[19]</sup> . . . . .	10
6	Local $\theta_{i,j}$ <sup>[19]</sup> . . . . .	10
7	First stage center of mass shift . . . . .	11
8	Tangential ogive nose . . . . .	12
9	Summary of Trajectory Phase . . . . .	13
10	Evasive maneuver . . . . .	13
11	Comparison of the Control Variable . . . . .	15
12	Results of the optimization process . . . . .	16
13	Comparison of Aerodynamic Models . . . . .	17
14	$C_p$ result of the paneling method for fixed Mach a null angle of incidence . . . . .	17
15	Structural results . . . . .	17
16	Maximum wall temperature over time for selected wall thicknesses <sup>[28]</sup> . . . . .	19
17	Temperature contours at re-entry burn conditions <sup>[28]</sup> . . . . .	19
18	Three types of retropropulsion modes <sup>[29]</sup> . . . . .	19
19	Rocket base plate and side wall heat flux distributions <sup>[29]</sup> . . . . .	20
20	Results of 1st Stage re-entry . . . . .	21
21	Heat flux and dynamic pressure profiles of first stage during re-entry . . . . .	22
22	Heat flux and dynamic pressure values of re-entry of second stage . . . . .	23
23	2D segmented schematic of launcher generated in OpenRocket with resultant dimensions	23
24	Axial Forces, Shear Forces, and Torque at max $q$ . . . . .	24
25	Downward shear force and bending moment . . . . .	26
26	Histogram of altitude and GLOM . . . . .	26
27	Results of the cost analysis and ROI computation . . . . .	27
28	House of Quality . . . . .	I
29	Performance Characteristics of Selected Liquid-propellant Engines <sup>[8]</sup> . . . . .	II
30	Trajectory parameters of Booster during re-entry . . . . .	VI
31	Re-entry booster acceleration components . . . . .	VII
32	Parachute limits <sup>[30]</sup> . . . . .	VII
33	First stage Mach profile during re-entry . . . . .	VIII
34	Heat flux profile of first stage during natural re-entry . . . . .	VIII
35	Grid Fins Configurations of Unswept (a), Locally Swept (b)(c) <sup>[38]</sup> . . . . .	VIII
36	Stage 2 re-entry parameters . . . . .	IX
37	SSO Trajectory Results . . . . .	X
38	Result of the Optimization Process SSO . . . . .	XI
39	Result of the Optimization Process SSO . . . . .	XI
40	Comparison of the Control Variable Equatorial Orbit . . . . .	XII
41	Result of the optimization process Equatorial Orbit . . . . .	XII
42	Comparison of Aerodynamic Models Equatorial Orbit . . . . .	XII
43	Structure Results Equatorial Orbit . . . . .	XIII
44	Result of the Optimization of Equatorial Orbit . . . . .	XIII
45	Result of the Optimization of Equatorial Orbit . . . . .	XIV
46	Result of the Optimization Process Equatorial Orbital . . . . .	XIV
47	Evolution of mean and standard deviation . . . . .	XV

## List of Tables

1	High level requirements . . . . .	1
2	Functional, operational and performance requirements . . . . .	1
3	Contributions to the $\Delta v$ budget . . . . .	3
4	Rutherford engines performance parameters <sup>[9]</sup> . . . . .	4
5	Combustion parameters . . . . .	4
6	Nozzle sizes . . . . .	4
7	Relevant results of the staging process . . . . .	8
8	Relevant results of the MERs process . . . . .	8
9	Calculation of $C_p$ based on profile zone for Mach $\leq 3^{[19]}$ . . . . .	11
10	Calculation of $C_p$ based on profile zone Mach $> 3^{[19]}$ . . . . .	11
11	Evasive maneuver input data . . . . .	13
12	Phase and Constraint Definition . . . . .	14
13	Stages of Booster Descent and Recovery . . . . .	19
14	Input data . . . . .	20
15	1st Stage re-entry landing targets . . . . .	21
16	1st Stage re-entry constraints . . . . .	21
17	Segmentation of the launcher . . . . .	24
18	Dimensions and sub-components within the discretized main modules . . . . .	25
19	Masses of the airplane . . . . .	25
20	Results Summary . . . . .	27
21	Main cost items of the launcher . . . . .	28
22	Mission Requirements Verification in the First Iteration . . . . .	28
23	Margins for tank volumes <sup>[8]</sup> . . . . .	III

# 1 Requirements and Functional Decomposition

## 1.1 Definition of Requirements

The requirements for this conceptual design are categorized according to their nature. The high-level requirements come from the customer and are divided into mandatory requirements (M), that state the minimal ones necessary to satisfy the customer's needs, and preference requirements (NH), which are evaluated to determine the "best" design, after the mandatory ones are respected. These specifications originate from the House of Quality (Figure 28 in Appendix A), marking the initial phase of our design process. This tool helps in identifying the system requirements, with the "Whats" specifying customer qualitative needs and the "Hows" defining engineering parameters to quantify them. Additionally, the HoQ benchmarks TERR-1 system against competitors on defined criteria, feasibility, and readiness. The results position TERR-1 as an innovative launcher, effectively meeting the customer's needs.

The following table summarizes the high level requirements of this mission:

REQ. ID	IMPORTANCE	REQUIREMENT	DESCRIPTION
TERR1-HLR-001	M	SAFE LAUNCH	The launch and the flight shall be unhazardous for both civilians and personnel
TERR1-HLR-002	M	RECOVERABILITY OF FIRST STAGE	The first stage of the launcher shall be recovered undamaged for following reuse
TERR1-HLR-003	M	TANDEM CONFIGURATION	The launcher shall employ a tandem configuration
TERR1-HLR-004	M	LAUNCH FROM CIVIL AIRCRAFT	The airborne launcher shall be deployed from a civil carrier
TERR1-HLR-005	M	TARGET ORBIT	The launcher shall inject the nominal payload in SSO and 400 kg of payload in LEO
TERR1-HLR-006	M	SMALL NUMBER OF REUSES FOR ROI	The design shall guarantee a small number of reuses for the ROI
TERR1-HLR-007	NH	RECOVERABILITY OF UPPER STAGES	The upper stages should be recovered for reusability
TERR1-HLR-008	NH	TOXICITY OF PROPELLANT	The propellant should have low toxicity level
TERR1-HLR-009	NH	SHORT TIME TO MARKET	The launcher should be delivered to the market in 4 years

Table 1: High level requirements

To fulfill the mission, functional, operational, and performance requirements are established: defining "what" must be done, "how" it must be achieved, and "how well" the requirement shall be satisfied. Table 2 contains the main requirements:

REQ. ID	REQUIREMENT	DESCRIPTION
TERR1-FR-001	AERODYNAMIC EFFICIENCY	Aerodynamic efficiency shall minimize the drag in the ascent phase
TERR1-FR-002	TRAJECTORY OPTIMIZATION	The trajectory shall minimize the propellant mass
TERR1-FR-003	SAFETY FACTOR	Safety factor shall ensure the launcher's reliability and the reusability of the first stage
TERR1-FR-004	LAUNCHER DIMENSIONS	The dimensions of the launcher shall be compatible with the carrier
TERR1-PR-001	PAYLOAD MASS	The payload mass shall be max 400 kg
TERR1-PR-002	TARGET ORBIT	The launcher shall inject the payload into a target altitude with an accuracy of orbit insertion within 10 km
TERR1-OR-001	RE-ENTRY	The launcher shall perform a re-entry and landing burn
TERR1-OR-002	DELTAV	$\Delta v$ budget shall allow the launcher to reach the nominal orbit and perform the first stage re-entry

Table 2: Functional, operational and performance requirements

## 1.2 Functional decomposition

In the conceptual design process, functional decomposition serves as an essential step for systematically breaking down system high-level functions into more specific ones. Figure 1 illustrates the functional decomposition, displaying the mandatory high-level requirements in the first row, followed by the functions the system must perform to fulfill each requirement.

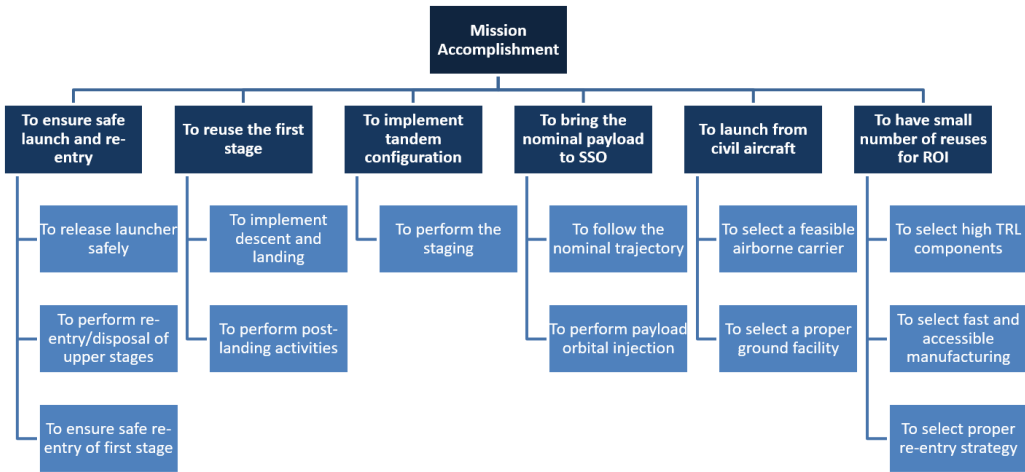


Figure 1: Functional decomposition

### 1.3 Baseline Selection

For the conceptual design of a new launch vehicle, the baseline is established by three proven systems. LauncherOne is selected for its airborne launch methodology, Electron is chosen for engine selection due to its innovative and lightweight Rutherford engines and Falcon 9 serves as the reference for the re-entry strategy, leveraging its demonstrated success in recovering and reusing rocket boosters. The major details of each selection and their implications are described in the respective Sections.

## 2 Mission Analysis

The objective of the mission analysis is to compute the  $\Delta v$  budget. This budget comprises several contributions, with a 2% margin added to the final value to account for uncertainties. The computation of these contributions is closely tied to the development of the launcher subsystems. Therefore, a preliminary estimation has been carried out to enable the initial subsystems design. The first contribution to the  $\Delta v$  budget is the velocity associated to the target orbit. According to the TERR1-HLR-005 requirement (Table 1), the mission targets a Sun-Synchronous Orbit (SSO) with an altitude of 400 km and an inclination of 98°. These parameters, along with an assumed eccentricity  $e = 0$ , have been used for the preliminary velocity computation.

Another contribution to the  $\Delta v$  budget is the effect of Earth's rotation. Since the target orbit is retrograde, the launch must be westward, resulting in an additional contribution to the velocity budget. This value depends on the latitude of the launch site: locations closer to the equator experience a larger negative impact due to the higher rotational speed of the Earth. To mitigate this effect, various launch sites have been evaluated, particularly those used by LauncherOne. Among these, Spaceport Cornwall (UK) has been selected, as it is the farthest from the equator, thereby reducing the impact of Earth's rotational velocity on the  $\Delta v$  budget.

An airborne launcher benefits from being carried by an aircraft, which provides an initial velocity  $v_0 \neq 0$  km/s. The initial velocity reduces the propellant required to reach the same speed compared to a vertical launch. This improvement positively impacts the  $\Delta v$  budget, enhancing efficiency. For this preliminary design phase, the chosen carrier is the Boeing 747-400, therefore its cruise velocity is used as a reference (see Section 7).

The remaining contributions to the  $\Delta v$  budget arise from losses due to gravity, aerodynamic drag, and steering. These values have been obtained from the literature<sup>[1]</sup>.

Another contribution would be the propellant required for the descent phase of the first stage, including re-entry and landing burns. However, this is omitted in the first iteration, as its estimation depends on the mass properties discussed in Chapter 4. Table 3 summarizes the values of the contributions mentioned above.

Contribution	Value (km/s)	Contribution	Value (km/s)
$\Delta v$ Orbit	7.682732	$\Delta v$ Carrier	0.294978
$\Delta v$ Earth Rotation	0.288915	$\Delta v$ Gravity	1.5000
$\Delta v$ Drag	0.1500	$\Delta v$ Steering	0.0500
Margin	0.187533	<b>Total <math>\Delta v</math></b>	<b>9.564203</b>

Table 3: Contributions to the  $\Delta v$  budget

## Carrier Selection

The Boeing 747-400 has been selected as the civil carrier, consistent with the LauncherOne system, and has been chosen during the mass definition process. With an estimated total system mass of 34 tons, a large carrier is essential. The Boeing 747-400 accommodates this need, supporting up to 38 tons when accounting for the LauncherOne pylon<sup>[2]</sup>. Its structural capacity has undergone preliminary validation in Section 7; however, detailed flight dynamics analyses are still pending.

Preliminary assumptions include a flight path angle of 30°, an altitude of 10 km, and a flight duration of 3 hours, based on procedures from Cornwall Spaceport<sup>[3]</sup>. While this choice satisfies the current requirements, further evaluations are recommended to explore alternative carriers that might enable higher altitudes or steeper flight path angles, potentially easing the design of other subsystems.

## 3 Propulsion System

The TERR1-HLR-009 requirement (Table 1) defines the design of the propulsion subsystem. The development, manufacturing, and testing of a rocket engine is an extensive process, often requiring over four years to complete. As a result, in-house engine development is deemed impractical. Therefore, to meet the requirement, an off-the-shelf engine is selected. The engine selection is further guided by TERR1-HLR-008 requirement (Table 1), which entails the use of a propellant combination with low toxicity levels.

### 3.1 Propellant Couple selection

The fuel selection criteria are  $I_{sp}$  and toxicity, which is a critical factor for the safe operation and maintenance of reusable engine systems. According to the baseline engine solution, the fuel choice is RP-1. This fuel is a highly refined kerosene, designed specifically for use as rocket propellant. Although it delivers less specific impulse than liquid hydrogen, meaning lower thrust per unit mass, RP-1 offers several practical advantages: it is significantly cheaper, can be stored at ambient temperature, is much denser, and poses a considerably lower explosive risk. RP-1's higher density offers more energy per volume than liquid hydrogen (LH2) and methane (LCH4). Its extensive refinement eliminates harmful compounds like sulfur, reducing engine damage and toxicity<sup>[4][5]</sup> while improving efficiency and safety. Impurities that cause coking and residue buildup are also removed, enhancing engine longevity and performance of the rocket engine. Although RP-1 combustion produces carbon dioxide (CO2), a contributor to atmospheric emissions, it remains safer to handle than hypergolic fuels and many other alternatives<sup>[6]</sup>. The selected oxidizer is LOX, as commonly used in typical applications with RP-1<sup>[7]</sup>.

### 3.2 Engine Selection

Based on a literature analysis, the Electron launcher developed by Rocket Lab emerges as a potential candidate for reusability. Its propulsion system relies on Rutherford engines, with the vacuum specific impulse and thrust values for both the first and second stages summarized in Table 4. A baseline analysis is conducted using these parameters. To evaluate engine performance, the ideal specific impulse values in vacuum are calculated using the NASA CEA code. These calculations assume typical expansion ratio values of 20 for the first stage and 100 for the second stage<sup>[8]</sup>, along with a combustion chamber pressure of 60 bar, a value derived from historical applications of LOX/RP-1 technology (Figure 29 in Appendix B)<sup>[8]</sup>. This approach enables the determination of the engines' actual specific impulse efficiencies, which in turn are used to estimate the real optimal specific impulse values.

Stage	$Isp_{vac}$ [s]	T [kN]	$Isp_{id,vac}$ [s]	$\eta$	$Isp_{id,opt}$ [s]	$Isp_{opt,re}$ [s]
I	311	24.91	337.9	0.9204	319.1	294
II	343	25.8	361.9	0.9478	350.1	332

Table 4: Rutherford engines performance parameters<sup>[9]</sup>

Based on the manufacturer's user guide, neither the dimensions nor the combustion chamber parameters are provided. Consequently, the nozzle dimensions are estimated by scaling available images, yielding reasonable values. Following this, and considering the LauncherOne's air-launch strategy, the expansion ratio of the first stage is estimated by applying the condition of optimal expansion at an altitude of 10 km (Eqs.21, 22 and 23 in Appendix B) according to the values reported in Table 5. The value obtained from this relation matched the typical first-stage expansion ratio of 20. Using this value, it's possible to compute the throat area. Then, by assuming a typical expansion ratio of 100 for vacuum conditions, the nozzle exhaust area for the second stage is approximated (Table 6).

Pc [bar]	Pe [bar]	k
60	0.2637	1.24

Table 5: Combustion parameters

De <sub>1</sub> [m]	Dt [m]	De <sub>2</sub> [m]
0.28	0.0626	0.6261

Table 6: Nozzle sizes

By evaluating the thrust per engine and the required total thrust, based on a fixed thrust-to-weight (T/W) ratio of 1.31 for the first stage and 1.15 for the second stage, the number of engines needed for each stage is determined. Although a more accurate thrust distribution could have been achieved by scaling the thrust values from sea-level conditions to air-drop conditions, the sea-level thrust was used to ensure a conservative design. This analysis resulted in 18 engines for the first stage and 3 engines for the second stage (Fig.2). Building the cluster configuration for the first stage, the 11+6+1 configuration is preferred as shown in Fig.2a. This is because it offers more lateral space for TVC (Thrust Vector Control) movement, but it also presents a more complex thrust structure<sup>[8]</sup>. Specifically, the thrust from the central engine needs to be redirected to the outer radius of the rocket, adding to the design complexity. Regarding the throttling capability of the engine, no official data have been found, so a 50% range is assumed, since it is a liquid rocket engine with electric turbopumps.

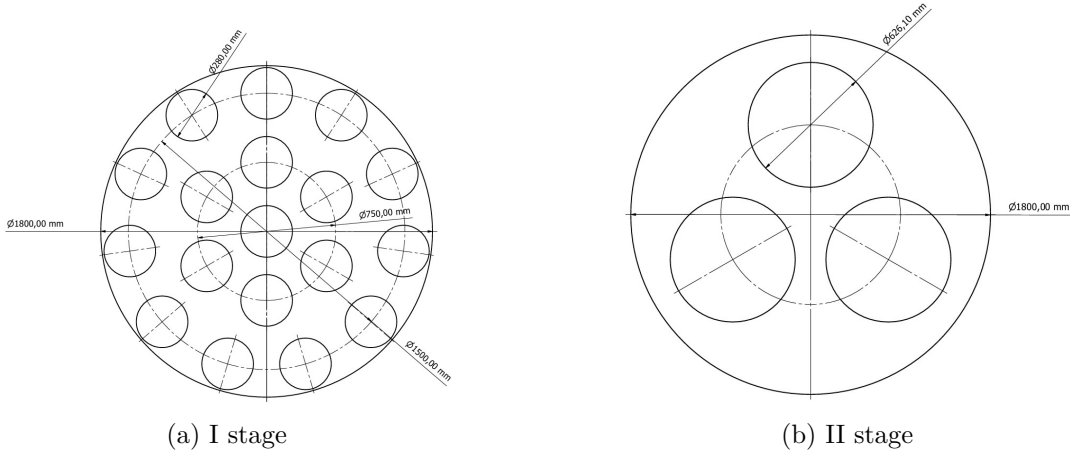
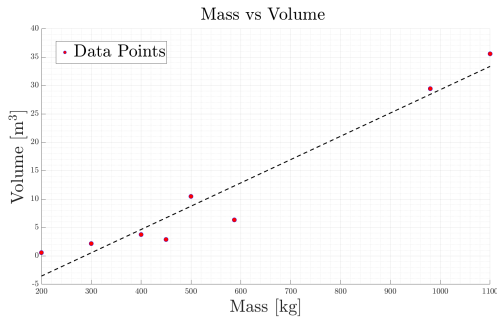


Figure 2: Cluster configuration

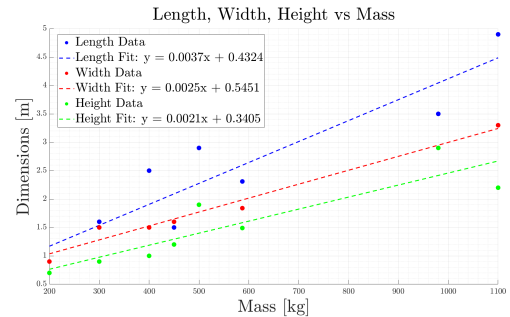
## 4 Masses

### 4.1 Preliminary Dimensioning

The diameter is the key parameter to begin with the launcher design. In order to define it, some data regarding payloads with different masses and dimensions have been collected<sup>[10][11][12][13][14][15][16]</sup>. A linear fit is used to approximate the average dimensions, based on two key considerations: the average payload volume and dimensions.



(a) Payload volume vs payload mass of different payloads



(b) Length, width, and height vs payload mass of different payloads

Figure 3: Payload dimensions estimation

Figure 3a yields a resultant volume of  $4.63 \text{ m}^3$  for a 400 kg payload whereas from Figure 3b, one can obtain a payload of  $1.91 \text{ m} \times 1.55 \text{ m} \times 1.18 \text{ m}$ . If the payload is assumed to be a cube, a  $1.67 \text{ m}$  edge length is required based on found volume. Therefore, a square base of  $1.67 \text{ m} \times 1.67 \text{ m}$  and a height of  $1.91 \text{ m}$  seems an adequate over sizing of the payload which can be carried by an ogive fairing of  $1.80 \text{ m}$  diameter and  $3.6 \text{ m}$  length. The fairing diameter determines the overall structure diameter of the TERR-1, as both the first and second stages share the same diameter.

The tank sizing is based on the stage diameter and the required propellant volume, assuming the tanks have a cylindrical shape with two dome-shaped caps. To the volume computed, a margin is added as presented in Table 23 in Appendix C.

## 4.2 Masses model

Two different approaches are taken into account to compute the various masses of the launcher: the staging process approach and the MERs & thickness computation one. The first method provides an overall distribution of the masses among the launcher stages, while the second calculates the masses of each relevant structural component. The second approach uses empirical equations as a first estimate, and then refines the calculations using the thickness computed in Section 7 to compare and verify consistency. After completing all the calculations, the results obtained from both methods should coincide.

### 4.2.1 Staging process

The staging process aims to allocate the masses across the different stages of the launcher based on a cost function to be minimized (see Section 4.2.2). In this project, a two-stage launcher is selected because, for a payload ranging from 250 kg to 400 kg and an air-launched vehicle, the mass advantages of a three-stage setup do not justify the increased complexity and risks. Furthermore, given the average vehicle size, a third stage would have very small dimensions and components, implying additional challenges for manufacturing and higher costs.

Within this case study, a reusable first stage is analyzed as detailed by Dresia<sup>[1]</sup>. A reusable first stage cannot exhaust its entire propellant supply during ascent. The specific quantity of propellant allocated for re-entry and landing burns is contingent upon the dimensions and mass of the first stage. Consequently, traditional staging optimization methodologies designed for expendable launch vehicles are inapplicable, requiring an alternative approach.

The calculations for the propellant mass of each stage, including the propellant designated for the first stage re-entry and landing burns, are elaborated upon as follows. These computations necessitate several input parameters: the payload mass, the specific impulse of the engines, preliminary estimates of the structural coefficients and the overall mission  $\Delta v$ . Furthermore, the  $\Delta v$  required for the re-entry and landing burns ( $\Delta v_{landing}$ ) must be computed.

The equations employed in the mass calculations are derived from the structural coefficient, in conjunction with the Tsiolkovsky equation. The equations are annotated with subscript  $i$  with  $i = 1, 2$  respectively for the first and second stages.

Initially, the calculations are conducted for the second stage, taking into account the actual payload mass of the launcher, denoted as  $M_{pay}$ . Following this, the calculations for the first stage are carried out, where  $M_{pay}$  now includes both the payload and the second stage masses.

For the  $i$ -th stage, the preliminary task is to determine the structural mass:

$$M_{S,i} = A_i M_{pay,i} \quad (1)$$

where

$$A_i = \frac{\epsilon_{s,i} - \epsilon_{s,i} \cdot n_i}{(1 - P_i) \cdot n_i \cdot \epsilon_{s,i} + P_i \cdot n_i - 1} \quad (2)$$

Consequently, the total propellant mass can be computed as:

$$M_{P,i} = M_{S,i} \frac{1 - \epsilon_{s,i}}{\epsilon_{s,i}} \quad (3)$$

then, the masses for the re-entry and for the ascent can be obtained.

$$M_{P,i,landing} = M_{S,i} \cdot \frac{1 - \epsilon_{i,landing}}{\epsilon_{i,landing}}, \quad M_{P,i,ascent} = M_{P,i} - M_{P,i,landing} \quad (4)$$

where

$$\epsilon_{i,landing} = \frac{M_{S,i}}{M_{S,i} + M_{P,i,landing}} = \left( \frac{M_{0,i}}{M_{f,i}} \right)_{landing}^{-1} = \exp \left( -\frac{\Delta v_{i,landing}}{I_{sp,i} \cdot g_0} \right) \quad (5)$$

and

$$M_{P,i,landing} = P_i M_{P,i} \quad (6)$$

Moreover, to finalize the model, it is essential to estimate the terminal velocity attained by the first stage immediately before the beginning of the landing burn. The resultant estimated velocity is:

$$\Delta v_{1,landing} = 1.5 \sqrt{\frac{2Mg_0}{\rho A C_d}} \quad (7)$$

where  $M$  is the mass left after burnout,  $A$  is the wet area during the fall,  $\rho$  and  $C_D$  are the air density and the drag coefficient that for simplicity are assumed constant during the re-entry and equal to  $1.112 \text{ kg/m}^2$  and  $1.5820$ .

This estimate considers the terminal velocity of a body descending linearly through a fluid, with a 1.5 factor added to account for the  $\Delta v$  required for the re-entry burn. It assumes constant air density and drag coefficient throughout the re-entry phase, reflecting the simplifications of this preliminary analysis. To assess these topics, a better description and more precise computations about the re-entry phase are provided in Section 6.3.

#### 4.2.2 Staging optimization

To optimally distribute the masses, a constrained optimization problem is solved using Matlab<sup>®</sup>'s built-in function `fmincon`. This involves varying different variables and applying the necessary constraints. The variables adjusted by the solver to minimize these objective functions are:  $n_1, n_2, P_1, \epsilon_{s,1}, \epsilon_{s,2}$ . After obtaining these values, it is possible to compute the masses of the structure, the propellant and the GLOM. An important remark that needs to be stated is that the obtained propellant mass is incremented considering a factor of 1.02 that takes into account residuals and boil off; ignition losses are also considered<sup>[8]</sup>. It is crucial to emphasize that subsequent to stage separation, a small  $\Delta v$  is essential for the proper detachment of the two stages of the launcher. In this initial iteration, the computed masses exclude the one required for detachment for simplicity sake. Future iterations should incorporate this mass into the model.

The optimization problem needs some constraints to produce feasible results, the selected ones are the following:

$$\Delta v_{ascent} - c_1 \log(n_1) - c_2 \log(n_2) = 0 \quad (8)$$

to ensure that the launcher has enough propellant to achieve the wanted orbital velocity,

$$\Delta v_{1,landing} + c_1 \log(\epsilon_{1,landing}) = 0 \quad (9)$$

to ensure that the launcher has enough propellant to perform the re-entry burns,

$$M_{S,1,MER\&t} - M_{S,1,staging} = 0 \quad (10)$$

$$M_{S,2,MER\&t} - M_{S,2,staging} = 0 \quad (11)$$

to ensure that the structural mass computed with the staging process and the one computed with the MERs & thickness method are the same.

The optimization problem yields varying solutions depending on the selected objective function. In this project, two objective functions have been employed to compare results and ultimately determine the most appropriate solution for the proposed problem:

- **GLOM:** consists in the sum of the masses of the two stages plus the payload mass. This function is chosen because optimizing the GLOM means having an overall lighter launcher which is a desirable result especially for an airborne launcher.
- **Expendable mass:** represents the sum of the structural mass for each stage, divided by the hypothesized number of reuses specific for that stage. This function is chosen because one of the requirements for the proposed design is a small number of reuses for the ROI (TERR1-HLR-006, Table 1).

#### 4.2.3 MERs & Thickness computation

The staging process tackles the distribution of the launcher's total mass, focusing purely on structural masses through the use of  $\epsilon_s$ . In this approach, structural masses are evaluated based on a component build-up method. Initially, an estimation process employs Mass Estimation Relationships (MERs). These estimations guide the computation of the minimum thicknesses required to sustain loads computed in Section 7. With these thicknesses, each component mass is analytically computed, multiplying the volume for the density of the material (Al-Lithium 2090-T83), and expected to align with those predicted by the MERs. If discrepancies arise, the process shall be repeated until the convergence criteria are fulfilled. This project conducts only the first iteration, verifying if the MER-estimated masses exceed those calculated with minimal thickness, implying that the thickness considered surpasses the minimum needed to support the loads. The description of the internal and external structural components can be found in Section 7.1.

The following section provides the results only for the MERs part, while the final check on the loads is done in Section 7.

- **MERs:** for the internal components the relationships can be found in Edberg-Costa<sup>[8]</sup>, while for the external components the masses can be computed using the surface area and an areal density equal to  $13.3 \text{ kg/m}^2$  for metallic structures<sup>[8]</sup>. All the external components are modeled as cylindrical shells except for tanks.
- **Thickness computation:** After the stress analysis the obtained minimum thickness is used to compute the minimum masses of the launcher. To do that, a material should be selected. The choice of material is done among isotropic materials that have the least number of failure modes compared to composites materials, thus simplifying the stress analysis. Consequently, their application may be deemed inappropriate during the preliminary design phase without a proper testing campaign. The selected material is therefore Al-Lithium 2090-T83 due to its lower density compared to other typical metals.

### 4.3 Staging results

The masses computed with the staging method are:

	EM		GLOM	
	I STAGE	II STAGE	I STAGE	II STAGE
$M_S [kg]$	1 600.94	909.18	1 487.24	941.60
$M_{P,ascent} [kg]$	33 634.77	3 414.23	25 673.1	5 680.86
$M_{P,landing} [kg]$	753.16	0	764.84	0
$n [-]$	5.8552	3.9454	3.813624	5.7674
$\epsilon_s [-]$	0.044484	0.21029	0.053258	0.142182
$\epsilon_{landing} [-]$	0.680063	1	0.66038	1
$\Delta v_{ascent} [km/s]$	5.0955	4.4687	3.85933	5.7049
$\Delta v_{landing} [km/s]$	1.11165	0	1.1963	0
$t_{b,ascent} [s]$	216.27	143.61	165.08	238.96
$t_{b,landing} [s]$	4.8424	0	4.1980	0
$L [m]$	18.77	5.4528	15.512	6.3841
$D [m]$	1.8	1.8	1.8	1.8
<b>GLOM [kg]</b>	40 562.29		34 797.62	
$L_{tot} [m]$	27.8318		25.4966	
$\Delta v_{tot} [km/s]$	9.564203		9.564203	

Table 7: Relevant results of the staging process

The results show that both methods enable the launcher to deliver the necessary  $\Delta v$  for the nominal mission while carrying a 250 kg payload. Given that the mission aims to achieve a Return On Investment in a limited number of reuses, optimizing the expendable mass might be advantageous because the algorithm seeks to maximize the allocation of structural mass to the reusable stage. However, initial analysis reveals that reducing expendable mass increases the GLOM. In this scenario, by prioritizing expendable mass optimization, the GLOM exceeds the one of the GLOM optimization by more than 5 000 kg, with a structural mass saving of under 50 kg in the second non-reusable stage. Therefore, for this initial phase of the design, optimizing the GLOM is selected because of its reduced mass which is the safest option. In future iterations, modifications to parameters such as materials, dimensions and internal components might make the expendable mass optimization approach yield more beneficial outcomes in terms of masses, considering also the benefits that this approach provides in terms of costs savings as better explained in Section 9.

### 4.4 MERs & thickness results

In this Section, the results obtained with the second approach are presented in Table 8, but only in the case of GLOM optimization.

INTERNAL COMPONENTS	MASS [kg]		EXTERNAL COMPONENTS	MASS [kg]
	I STAGE	II STAGE		
LOx tank insulation	50.64	14.35	Fairing	109.66
Thrust structure	114.34	19.73	Second stage forward skirt	110.26
Avionics	15	60	Second LOx tank	42.02
Wiring	22.18	9.13	Inter-tank	165.40
Gimbal mechanism	25.06	4.18	Second RP-1 tank	25.94
Engine	476.76	145.53	Aft skirt	110.26
Pump	80.98	80.98	Inter-stage	132.32
-	-	-	First LOx tank	195.57
-	-	-	Inter-tank	165.40
-	-	-	First RP-1 tank	120.76
-	-	-	Aft skirt	132.32
Internal structural mass	784.99	333.89	External structural mass	1 309.97
Total structural mass [kg]			2 428.85	

Table 8: Relevant results of the MERs process

The results show the division of the structural mass into internal and external components using the MER method. It is important to note that the final launcher will integrate additional components not included in this preliminary design. However, as the design evolves, a more detailed component analysis will be necessary. Additionally, it is evident that the structural mass, derived by summing the masses of all individual components, matches the mass determined through the staging approach. This alignment is crucial for ensuring the validity and consistency of both methods.

## 5 Aerodynamics

Considering the high dynamism of the initial design phase, the aerodynamics subsystem has to be developed accordingly, evaluating both accuracy and computational time.

To investigate the aerodynamic configuration of the launcher, the Jørgensen Allen equations are applied due to their convenient computational cost and their flexibility with respect to the angle of attack. Such constraints are both dictated by the iterative nature of the study case and the re-entry condition where atmospheric drag is exploited to decelerate the launcher. At the same time, a panel method is implemented, not included in the iterative trajectory analysis, to have a better insight into structural loads and aerodynamic efficiency. Such a method is particularly suitable for preliminary design due to its faster computational capabilities, compared to Computational Fluid Dynamics (CFD), to its versatility for complex geometry and finally to its accuracy. However, the panel method is only employed for the supersonic regime considering that the LV operates for the largest part in this flight condition.

Furthermore, to properly grant stability, fins are taken into account and their sizing is strictly related to the stability margin, but constrained by the carrier geometry and structural feasibility. Their length is set equal to the launcher diameter, while their opening angle is  $20^\circ$ , to avoid flow separation<sup>[17]</sup>. Furthermore, also the tanks allocation is optimized in order to diminish the aerodynamic destabilizing torque as subsequently explained.

### 5.1 Jørgensen-Allen approach

The implemented equations are those described by Jørgensen<sup>[18]</sup>. Therefore, a component build-up approach is preferred to estimate the overall aerodynamic forces. The aim is to estimate the lift and drag coefficient, respectively  $C_L$  and  $C_D$ , through linearized theory. The problem can be reformulated in axial  $C_a$  and normal  $C_n$  coefficient evaluation. Moreover, the  $C_a$  can be considered as the sum of three different factor: base-drag, skin friction and nose contribution. Consistently with the expectation, such coefficients depend simultaneously on shape, geometry and flight condition. Finally, the aerodynamic forces can be expressed as a function of time, as the flight condition varies temporally along the trajectory.

### 5.2 Panel Model Central body approach

The panel method employed has been formulated and validated by Mancini<sup>[19]</sup>. This methodology is based on the appropriate application of different aerodynamic models in relation to the Mach number and local incidence angles  $\theta_{i,j}$  (see Figure 6). The initial phase requires establishing a three-dimensional model for the axial-symmetric LV and generating a mesh on its surface. Panels have been discretized along both the longitudinal and radial directions, and can be distinguished through their respective indices  $i, j$  and thus associated with their normal out-of-plane vector. Furthermore, to ensure consistency with the employed methods, the mesh generation process must approximate locally round-shaped surfaces as a succession of cones<sup>[20]</sup> (see Figure 5).

Consequently, knowing the relative wind vector, it is possible to compute the local incidence angle with respect to the panel:  $\theta_{i,j}$ . This modeling and mesh generation approach is critical for accurately simulating the aerodynamic forces and moments acting

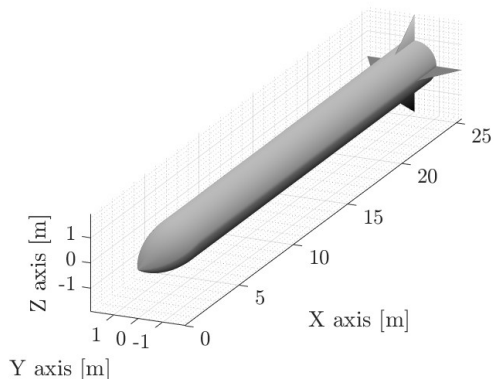


Figure 4: 3-D Launcher model

on the launcher. The use of discrete panels allows for precise computation of pressure distributions and flow interactions, which are essential for designing and analyzing the *LV*'s stability and performance during ascent.

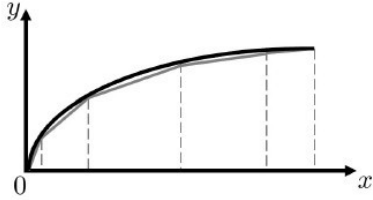


Figure 5: Local cone approximation<sup>[19]</sup>

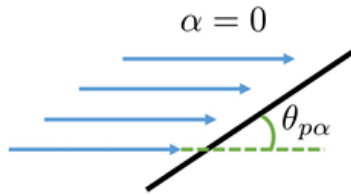


Figure 6: Local  $\theta_{i,j}$ <sup>[19]</sup>

However, the panels related to a negative  $\theta_{i,j}$  are neglected in the force computation since they are not directly invested by the flow. This can possibly lead to a mismatch among the obtained forces and the physical outcomes in case of high angle of attack, although not considered at this design phase. Considering upwind panels it is possible to compute the local pressure coefficient  $C_p$ .

The next step is the estimation of the local  $C_p$  coefficient where multiple methods are combined in order to have accurate data and reasonable computational time with respect to CFD. Such results can be obtained in this study case, considering that the method is stiff for small angle of attack. Also the fins are evaluated with the panel method and a more detailed description is in Section 5.2.4.

### 5.2.1 Modified Newton method

The Modified Newton theory enables to estimate the local  $C_p$  considering high  $\theta$  and enhances its validity as the Mach increases.

$$C_{p_{i,j}} = C_{p_{max}} \sin^2 \theta_{i,j} \quad (12)$$

Where  $C_{p_{max}}$  is computed at the stagnation point subsequent to the up-front normal shockwave, as shown below:

$$C_{p_{max}} = \frac{P_0 - P_\infty}{\frac{1}{2} \rho_\infty v_\infty^2} = \frac{2}{kM^2} \left( \frac{P_0}{P_\infty} - 1 \right) \quad (13)$$

where  $P_0$  is the total pressure, while the  $\infty$  subscript refers to the reference value of the unperturbed field. Such a method is considerably suitable to analyze the "leading" cone meshes.

### 5.2.2 Krasnov Equation

The Krasnov equation is adopted as link between the supersonic and the Modified Newton method, due to the inapplicability of the second at lower  $\theta_{i,j}$ . Moreover, the Krasnov can be extended up to 50° of semi-apex angle of the cone and Mach 8, as the case in study (see Figure 12a). Indeed, higher Mach are obtained at altitudes where the atmospheric interferences can be neglected<sup>[21]</sup>.

$$C_{pKr_{i,j}} = \left( 0.0016 + \frac{0.002}{M_\infty^2} \right) \cdot (\theta_{i,j}^{1.7}) \quad (14)$$

### 5.2.3 Supersonic method for slender bodies

The supersonic source method for slender bodies enables each panel to be influenced by the others included into the same Mach cone<sup>[19]</sup>. However, this model can be evaluated from an initial physical point, defined as  $\xi_1$ , which represents an upper limit of validity and applicability. Necessarily, each panel is associated to a certain  $\xi_i$  value and due to the axial symmetric body it can be computed as:

$$\xi_i = x_i - \beta r_i \quad (15)$$

where  $r_i$  is the local radius of the body at the  $i$ -th mesh position along the LV longitudinal axis while  $\beta = \sqrt{M_\infty^2 - 1}$ . Afterwards, it is possible to compute the complete set of  $\xi$  values and the local velocities for the downward meshes, thus the  $C_{p_{i,j}}$  as reported by Mancini<sup>[19]</sup>.

To reduce computational cost, the supersonic source method is applied only for  $1 < M < 3$ , as  $\xi_1$  moves too far along the x-axis due to the Mach cone's stretch, rendering its application outside this range

ineffective. The detailed analysis of the  $C_p$  distribution along the LV body enables the calculation of the total aerodynamic forces by integrating over the surface areas and considering the local pressure applied at the centroid of each panel.

An overview of the illustrated method is present in the following tables:

Profile zone	Range	Method
I	$0 < x   \theta(x) = 35^\circ$	Newton modified theory
II	$x   \theta(x) = 35^\circ < x \leq \xi_1$	Krasnov's equation
III	$\xi_1 \leq x \leq L$	Supersonic source method

Table 9: Calculation of  $C_p$  based on profile zone for  $Mach \leq 3^{[19]}$

Profile zone	Range	Method
I	$0 < x \leq x   \theta(x) = 35^\circ$	Newton modified theory
II	$x   \theta(x) = 35^\circ < x \leq L$	Krasnov's equation

Table 10: Calculation of  $C_p$  based on profile zone  $Mach > 3^{[19]}$

It is important to highlight that the transitioning from zone I to II is determined by the panel's local incidence, whereas the shift from zone II to III is dictated by the  $\xi_1$ .

#### 5.2.4 Fin panel method

A supersonic source method for triangular wings<sup>[20]</sup> is employed as a preliminary evaluation of aerodynamic loads. In this approach, the entire surface is represented by a distribution of sources. The computations are performed for each panel, and the aggregated results yield the overall coefficient of pressure ( $C_p$ )<sup>[20]</sup>.

#### 5.2.5 Aerodynamic results

The LV shape (see Figure 4) is strictly compelled by both the payload size and the thermal load analysis carried in Section 6. Moreover, even the generated drag has to be taken in account, leading to an overall compromise. While the diameter reduction alleviates both  $\Delta v$  losses and structural loads, it is unfeasible with respect to an average payload size compared to the requested one. Subsequently, the diameter results in  $d = 1.8\text{ m}$  which directly affects the launcher length, compelled by the propellant volume. Additionally, a larger diameter reduces the aeroelastic effects, improves the control performances and the packaging. In the initial analysis, designs without shoulders or boattails are considered, despite that boattails are more efficient in subsonic flight than in supersonic and can negatively affect control performance. Moreover, the rocket can be considered as a slender body and through the evaluation of aerodynamic stability margin, detailed below, triangular fins, as first assumption, are posed at the LV tail. However, these devices are constrained in size, in fact they are both limited by the allocation underneath the carrier and the structural loads, considerably relevant at max  $q$  condition. The stability constrained is not investigated for the second stage, due to high altitude (see Figure 13b), which ensures the absence of meaningful aerodynamic forces. Lastly, it is possible to have an initial estimate of the SM through the Barrowman equation (see Eqs.43-49 in Appendix D.1), at the launcher release which is the most critical condition due to the LV aerodynamic instability,  $SM = -6.5681$ . Therefore, at the initial launcher detachment, a nose-up torque is applied. Although no fin deflection control or SAS control method is implemented in this design phase, it should be considered in a more detailed analysis.

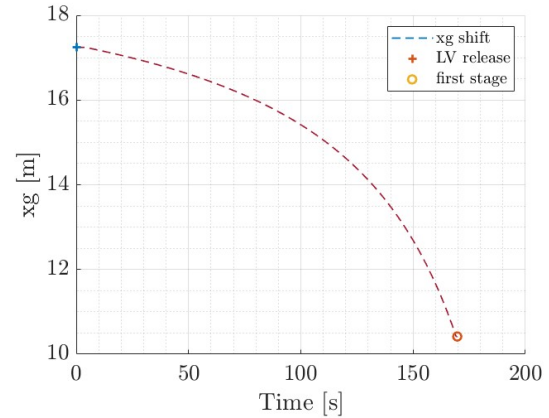


Figure 7: First stage center of mass shift

Specifically, it is possible to implement a SAS that involves both control surfaces and TVC to stabilize the LV during the ascent phase, which is critical from the stability viewpoint. As for the nose geometry, a tangent ogive shape is chosen with a design fineness ratio of 2<sup>[17]</sup>, as a compromise between aerodynamics and LV size (Figure 8). While it causes slightly higher drag compared to a conical nose, it ensures detachment of the frontal bow shockwave from the body. This design choice reduces tip temperature and avoids excessive structural thermal damages, as detailed in Section 6. Lastly, a wingless shape is chosen considering the high dynamic pressure working regime, carrier compatibility and weight saving.

Proper mesh discretization should also be evaluated to avoid discontinuities between meshes.

In summary, while the tangent ogive nose geometry provides aerodynamic benefits and thermal protection, further detailed analyses are necessary to optimize control mechanisms and structural design.

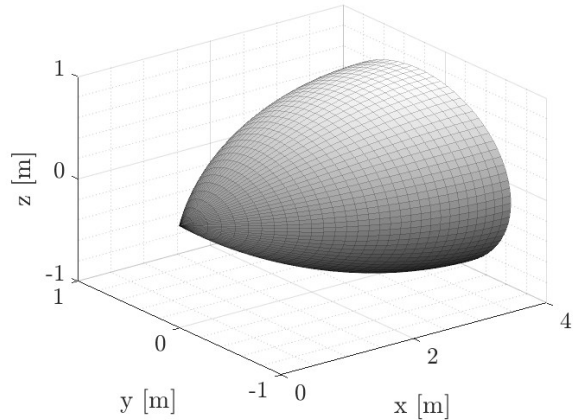


Figure 8: Tangential ogive nose

## 6 Trajectory

### 6.1 Introduction

Once the staging and propulsion parameters are computed, the next step is to evaluate whether these values enable the launcher to achieve the desired orbit efficiently. To achieve this, an optimization model is implemented to simulate the rocket's ascent trajectory. This simulation provides preliminary results, including the nominal trajectory during this initial iteration.

All the analyses are performed under the point-mass assumption, which simplifies the dynamics while still providing valuable insights. More precisely, the trajectory design for this launcher includes a brief ballistic phase which uses a gravity turn maneuver to reduce the flight path angle, aligning the velocity vector with the orbital plane and minimizing any undesirable vertical velocity component. This approach mirrors the trajectory strategies employed by LauncherOne<sup>[22]</sup>, which uses a small coasting phase between the two burns of its second stage. By adapting such techniques to the two-stage system presented in this report, the aim is to maximize orbital insertion accuracy while minimizing energy losses.

Furthermore, a preliminary analysis is carried out to evaluate the feasibility of a vertical landing for the first stage as re-entry strategy. The results are essential to assess the booster's reusability and overall mission cost-efficiency, aligning with the requirements and the modern trends in space launch systems.

### 6.2 Ascent phase

In this preliminary analysis, the trajectory is designed to validate the results obtained from other subsystems. The primary objective is to streamline the workflow for better understanding of the problem during this initial iteration, laying a foundation for future design improvements.

The problem is divided into 5 phases, as depicted in the Figure 9.

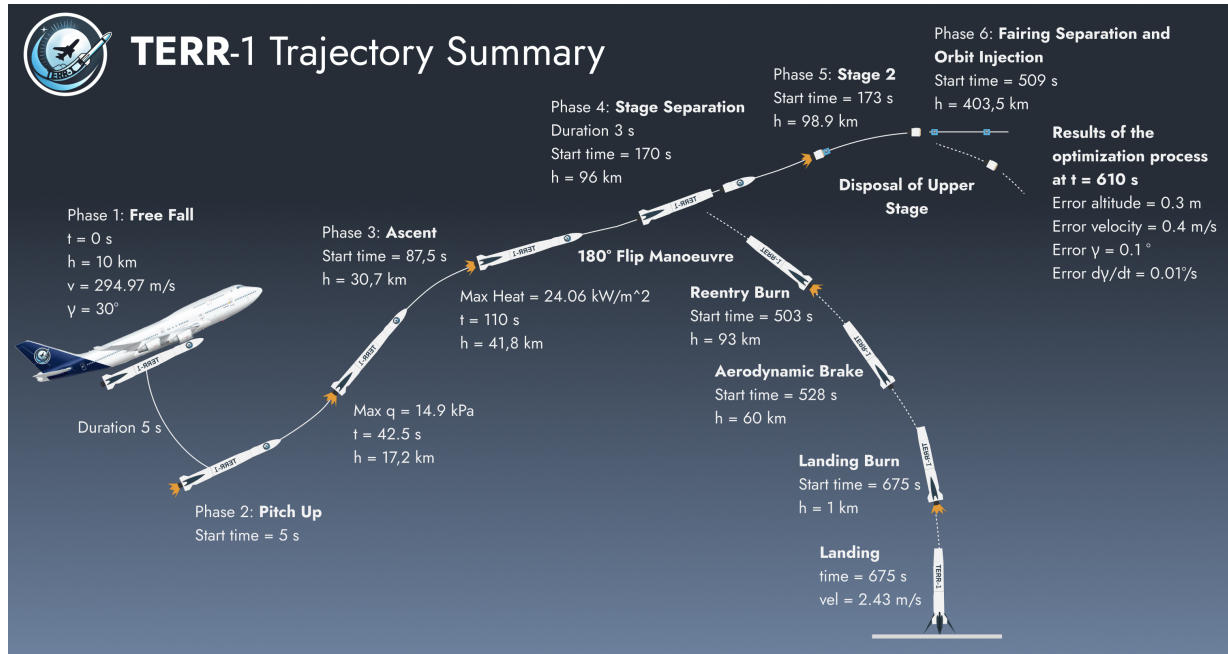


Figure 9: Summary of Trajectory Phase

### 6.2.1 Evasive maneuver

In an airborne launch system, the carrier aircraft is in charge of delivering the launcher to the optimal release altitude and inclination. Given the Safe Launch high-level requirement (TERR1-HLR-001), a preliminary analysis is conducted to model the aircraft's dynamics and its interaction with the launcher during the release phase. Once the launcher begins its free fall phase, the carrier performs an evasive maneuver to prevent any risk of collision with the rocket. The dynamics is implemented using a simplified point-mass turn maneuver model for the aircraft. Two carrier-related angles are considered:  $\theta$  and  $\phi$ , respectively the pitch and the bank angle. During this phase, the pitch angle  $\theta$  is assumed constant to simplify the modeling of the turn dynamics. This approach allows to approximate the carrier's trajectory, ensuring sufficient separation between the aircraft and the launcher after its release. The resulting trajectory, shown in Figure 10, is computed using Eqs. 50, 51 and 52 in Appendix E.1, with input data reported below:

$\theta$	$\phi$	Free fall time	Airplane velocity
$20^\circ$	$10^\circ$	5 s	294.97 m/s

Table 11: Evasive maneuver input data

### 6.2.2 Modeling approach

A 2D Earth-round model with a non-rotating reference frame is assumed for the analysis<sup>[23]</sup>. The governing equations (Eqs. 53 and 54) are expressed in the Appendix E.2.

In Section 5, two methods, Jørgensen and paneling, are implemented. However, for computational reasons, only the Jørgensen model is used during the optimization process, with the results verified in the post-processing phase, as discussed in Section 6.2.3. The aerodynamic contribution is turned off after 84 km because its effect on the dynamics becomes negligible. Drag  $C_D$  and lift  $C_L$  coefficients

are obtained from the aerodynamics subsystem. Atmospheric properties are modeled using Matlab<sup>®</sup>'s built-in function `atmosisa` below 84 km and an exponential model density<sup>[24]</sup> above this altitude. Static thrust contributions are not considered for simplicity.

The initial conditions are set as:

$$x_0 = \begin{bmatrix} v_0 = \Delta v_{carrier} = 294.97 \text{ m/s} \\ \gamma = 30^\circ \\ r = R_\oplus + 10 \text{ km} \\ \omega = 0^\circ \\ m = GLOM \end{bmatrix}, \quad \text{Target} = \begin{bmatrix} z_f = 400 \text{ km} \\ v_f = v_{\text{orbit}} + v_{\text{Earth}} \\ \gamma_f = 0^\circ \\ \dot{\gamma} = 0^\circ/\text{s} \end{bmatrix}$$

The target condition aims to achieve a Sun-Synchronous Orbit (SSO) at an altitude of 400 km. Due to the preliminary nature of the model, contributions such as Earth's rotation and plane-change maneuvers are simplified. Earth's rotational velocity, which must be countered to reach a near-polar orbit, is considered part of the target velocity instead of being considered a contribution for the initial velocity of the launcher. For optimization, the launch site of Spaceport Cornwall (UK) (lat = 50.5°N, long = 4.99° W) is selected to minimize this contribution. The rotational velocity contribution is calculated as  $v_{\text{Earth}} = 465.1 \cos(\text{lat}) \text{ m/s}$ .

Future models should incorporate these factors for a more accurate trajectory and  $\Delta v$  estimation.

### Event Handling and Phase Management

The simulation handles phase transitions automatically using event functions. Events are triggered by the depletion of propellant in a stage or the completion of a predefined phase duration controlled by time. The phase and time definitions are provided in Table 12.

The first phase involves a free-fall of 5 seconds to ensure safe separation from the carrier (see Section 6.2.1). During this phase, no thrust is applied, and it is assumed  $\dot{\gamma} = 0$ , considering a simple control through aerodynamics, which needs to be developed in future phases of the design.

Stage separation is modeled by updating the state vector to account for the reduction in inert mass and propellant. A clearance maneuver is implemented, applying a negative impulse ( $\Delta v = -3 \text{ m/s}$ ) to the first stage to avoid collisions. After a 3-second delay, the second stage ignites. Same procedure for the fairing separation needs to be considered. Future work will refine this phase to meet safety and collision-avoidance requirements and better inquire on the second stage disposal.

### Optimization Model

The trajectory optimization is based on Avio<sup>[25]</sup>, utilizing Matlab<sup>®</sup>'s built-in function `fmincon` with control nodes introduced at each phase to enhance the control variables and improve convergence. The control variables are then linearly interpolated between the nodes to ensure smooth temporal behavior. The cost function is defined as:

$$\min J = 0.6\Delta v_{\text{tot}} + 0.4e_{\text{target}} \quad (16)$$

The cost function minimizes the error relative to the target position ( $e_{\text{target}}$ ) to improve convergence, while reducing the  $\Delta v$  required for orbital insertion. The control variables include the gimbal angle  $\delta$  and throttling capability. Constraints are set to meet mission requirements with a tolerance of  $10^{-2}$ . These constraints are derived from literature and inputs from other subsystems in this work, and are summarized in Table 12.

Phase	Name	Stage	Time Duration	Point of Control	Constraint
1	Free Fall	1	5 s	1	$\dot{\gamma} = 0, T = 0$
2	Pitch Up	1	$t_{b1}/2$	3	$\max q \leq 35 \text{ kPa}$
3	Ascent	1	$t_{b1}/2 \leq t \leq t_{b1} + 10 \text{ s}$	3	
4	Stage Separation	—	3 s	—	$T = 0$
5	Stage 2	2	$t \leq t_{b2} + 100 \text{ s}$	12	
6	Orbit Injection	—	—	—	Target

Table 12: Phase and Constraint Definition

An important note is that the gimbal angle is not constrained by its typical  $15^\circ$  limit, as this is a preliminary feasibility assessment for the project. Additionally, the angle of attack  $\alpha$  is assumed to be zero during this initial analysis. This is a strong assumption that will be further discussed in Section 6.2.3, but it has been made to ensure consistency with the initial design of the other subsystems. The time durations for phases 3 and 5 have a slight margin to allow the optimization to throttle the engine according to the event phase detection. The throttling capability is limited between 50% and 100%, as described in Section 3.

Future developments should consider implementing a multiphase optimizer to optimize phase durations and include additional control points for enhanced performance.

### LEO Equatorial Orbit

To fully meet the requirement TERR1-HLR-005 (Table 1), the optimization code is tested using an equatorial launch from Kourou (Lat:  $5.15^\circ\text{N}$ , Lon:  $52.64^\circ\text{W}$ ), targeting a circular equatorial orbit. A 500 km altitude orbit is selected, with a payload of 400 kg. The Earth's rotational velocity at the launch site, calculated as  $v_{\text{Earth}} = 465.1 \cos(\text{lat}) = 463.22 \text{ m/s}$ , is incorporated into the target conditions. Additionally, the payload mass is increased from 250 kg to 400 kg to evaluate performance under updated conditions. The resulting initial and target parameters are summarized below:

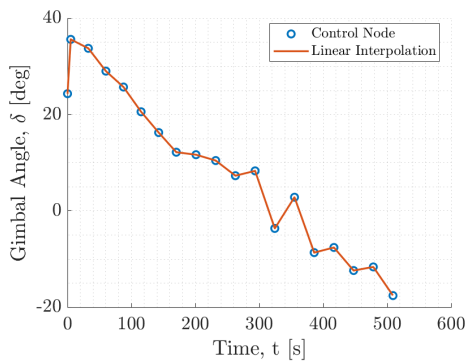
$$x_0 = \begin{bmatrix} v = \Delta v_{\text{carrier}} = 294.97 \text{ m/s} \\ \gamma = 30^\circ \\ r = R_\oplus + 10 \text{ km} \\ \omega = 0^\circ \\ m = GLOM + 150 \text{ kg} \end{bmatrix}, \quad \text{Target} = \begin{bmatrix} z_f = 500 \text{ km} \\ v_f = v_{\text{orbit}} - v_{\text{Earth}} \\ \gamma_f = 0^\circ \\ \dot{\gamma} = 0^\circ/\text{s} \end{bmatrix}$$

#### 6.2.3 Optimized Trajectory results

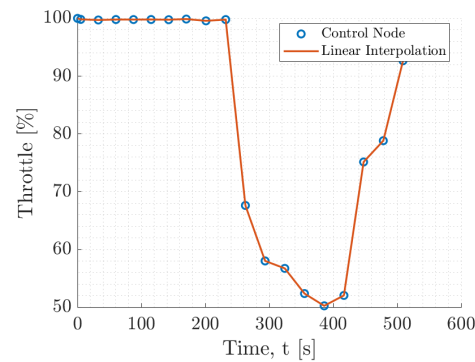
This section presents the results and corresponding considerations on the optimized trajectory. The analysis begins with the control variable results, specifically focusing on throttle and gimbal angles.

#### Control Variables and Result

As shown in Figure 11a, the gimbal angle exceeds its operational limit of approximately  $15^\circ$  during the initial phase, driven by the need to escape Earth's atmosphere and achieve a sufficient flight path angle,  $\gamma$ . This issue could be mitigated by refining the model to account for the angle of attack,  $\alpha$ . In the current model,  $\alpha$  is set to zero, which neglects any lift contribution that could help increase  $\gamma$  and facilitate reaching orbit. For example, the Pegasus system uses a first stage with aerodynamic surfaces to generate additional lift<sup>[26]</sup>. This limitation forces either an excessively high thrust requirement or the exploration of alternative methods to increase lift and achieve the desired orbit.



(a) Gimble Angle



(b) Throttle of the Engine

Figure 11: Comparison of the Control Variable

The optimizer recommends maximizing thrust during the first stage and the early portion of the second stage, followed by a gradual reduction during the latter part of the second stage. This strategy suggests the potential to slightly extend the burning time, however, this adjustment is constrained by

the altitude of the first-stage separation. In this case, stage separation occurs at approximately 96 km, which is relatively high compared to competitors that typically separate between 60 and 80 km. This difference arises from the need to compensate for the absence of lift contribution in the model. To achieve orbit under these conditions, the first stage burning time must be extended to reach the target orbit, resulting in a significant increase in the Gross Lift-Off Mass (GLOM) (see Sections 4, 10).

With the implemented control variables, the solution converges within the constraints. Below, plots of velocity and altitude are provided in Figure 12. In this simulation, the trajectory is integrated as ballistic, ignoring the maneuvers for the re-entry better discussed in subsection 6.3. Additional plots, such as thrust, angular position of the radius, radius, percentage in the tank of propellant, mass are included in the Appendix E.5 (Figure 39). For future iterations, it is crucial to better estimate the various losses in the trajectory. This will enable a more accurate calculation of the  $\Delta v$  budget, which is essential for refining mass estimations. A first estimation can be done by integrating loss during the trajectory<sup>[8]</sup>. However, steering losses are significantly higher due to the substantial control inputs required, as determined by the selected model.

$$\begin{aligned}\Delta v_{\text{drag}} &= \int_0^{t_f} \frac{D}{m} dt = 59.18 \text{ m/s}, \quad \Delta v_{\text{gravity}} = \int_0^{t_f} g \sin(\gamma) dt = 1402.18 \text{ m/s}, \\ \Delta v_{\text{steering}} &= \int_0^{t_f} \frac{2T}{m} \sin^2\left(\frac{\delta}{2}\right) dt = 415.29 \text{ m/s}.\end{aligned}\quad (17)$$

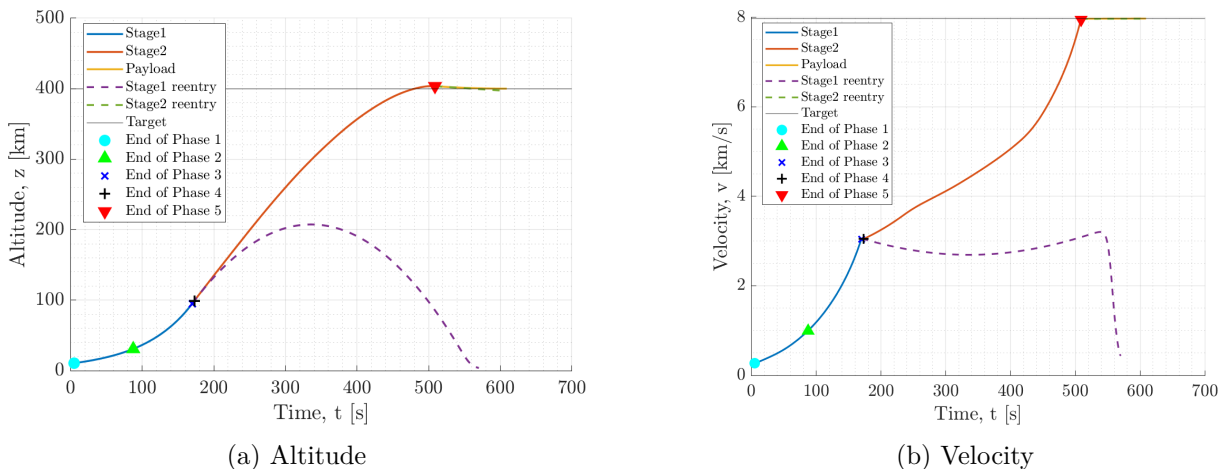


Figure 12: Results of the optimization process

### Comparison with Aerodynamic Models

This section also includes a comparison of aerodynamic results obtained through different methods. Aerodynamic forces are calculated using Jørgensen method during the integration due to lighter calculations, permitting the optimization to converge in a reasonable time. The results is compared in post processing with the paneling method in Figure 13.

As indicated in Figure 14, in line with the theoretical expectation<sup>[17][21]</sup> the  $C_p$  magnitude diminishes along the body starting from the nose and turns negative at the nose/central body joint. Indeed, in supersonic conditions, an expansion fan is generated, causing a negative  $C_p$ , strictly followed by a pressure recovery. Furthermore, as the Mach increases, the previous mentioned expansion does not take place anymore, making the  $C_p$  tend asymptotically to zero. Furthermore, the low Drag and  $C_p$  are justified by the cone shape, whose semi-apex angle is  $14^\circ$ . Moreover, the  $C_d$  trend is shown in Figure 13a. In particular, the initial inflection of the  $C_d$  can be justified by the Mach decrease during the free fall. Subsequently, the LV rapidly achieves its maximum Mach considering the almost transonic starting regime. It is worth to underline how even a slightly increase of the cone size results in a considerably drag increase. Due to the rarefied atmosphere, the aerodynamic forces are considered null after 84 km of altitude.

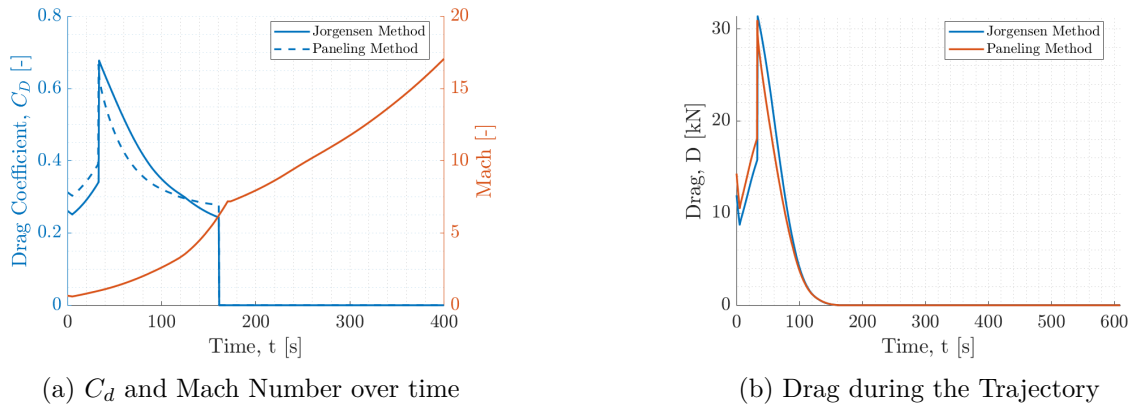
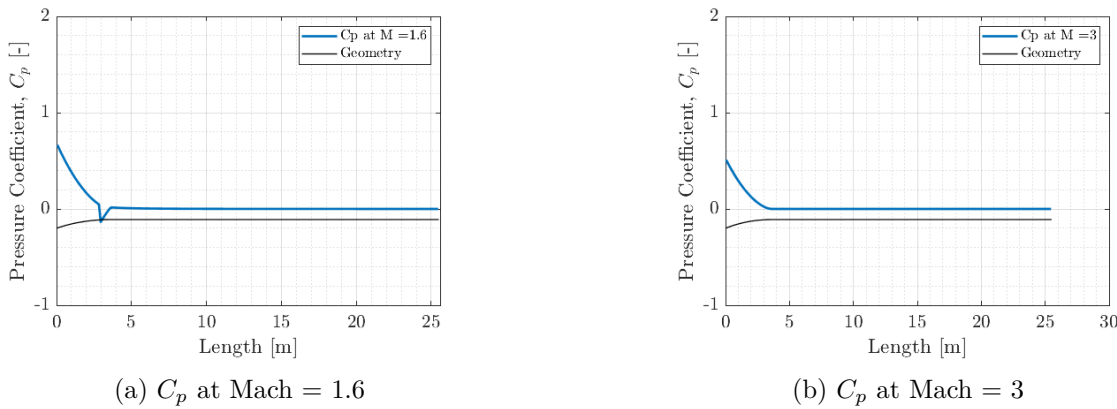


Figure 13: Comparison of Aerodynamic Models

Figure 14:  $C_p$  result of the paneling method for fixed Mach a null angle of incidence

## Structural Considerations

From a structural perspective, acceleration and maximum dynamic pressure ( $\max q$ ) conditions are calculated and compared to the throttling settings. Plots illustrating these results are provided below in Figure 15.

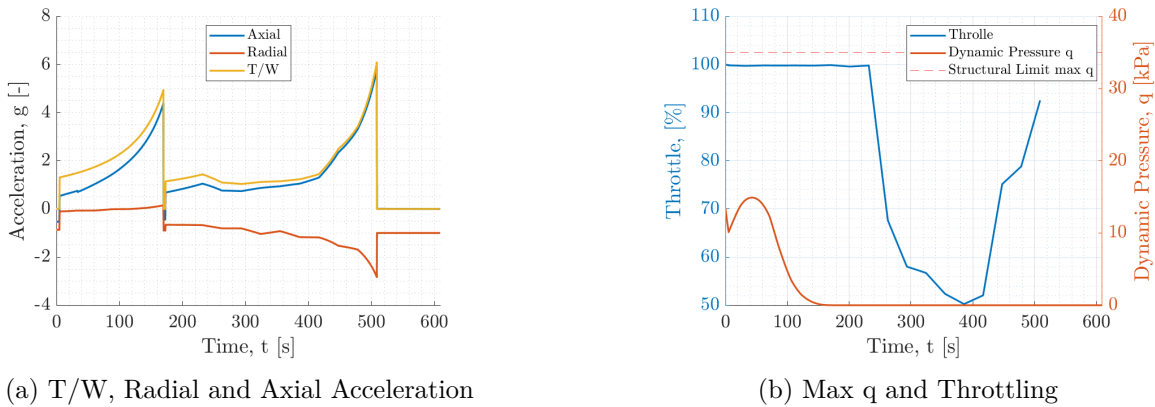


Figure 15: Structural results

$\max q$  remains well below the constraint of 35 kPa, eliminating the need for throttling to reduce stress. The resulting acceleration is consistent with real-world cases<sup>[8][22]</sup>, and has been verified in the structural analysis.

A check has also been performed for the thermal load during ascent. An estimation of the heat flux,  $\dot{q}$ , is calculated using the modified Chapman Eq.18, yielding a maximum result of approximately  $24.06 \text{ kW/m}^2$  at  $t = 110 \text{ s}$  (see Appendix E.5, Figure 39b), which is feasible for the limit of  $200 \text{ kW/m}^2$ <sup>[27]</sup> set for the TERR-1 system. A more accurate estimation should be performed in future analyses using CFD simulations.

## Equatorial Orbit Optimization

The equatorial orbit are achieved with acceptable error margins using the same optimization process. Comprehensive plots for these results are included in the Appendix E.6 for reference.

### 6.3 Re-entry of First stage

In this preliminary design phase, two re-entry strategies for the booster (first stage) are compared to determine the optimal approach to meet the customer requirements of reusability (TERR1-HLR-002) while maximizing ROI, within a limited number of reuses, and short time to market (TERR1-HLR-009). Initially, a parachute based re-entry strategy appeared to be a promising option due to its simplicity and reliance on proven technologies. However, further analysis revealed significant drawbacks specific to the TERR-1 system. These include a lack of control over re-entry and landing trajectories, high sensitivity to environmental conditions, criticalities for structural integrity after the impact and therefore the necessity for sea-water landings, which could cause corrosion and require extensive refurbishment, increasing ground operation costs as well as turnaround time<sup>[8]</sup>. These factors outweigh the advantages of a less complex system such as the parachute.

Furthermore, from a physical standpoint, the trajectory optimization conducted for TERR-1 indicates that the optimal staging occurs at an altitude of 96 km with a velocity of 3.03 km/s (see Section 6.2.3). Under these conditions, the booster re-entry velocity in the denser part of the atmosphere, where a parachute system could be deployed, is excessively high, resulting in thermal fluxes exceeding 200  $kW/m^2$ , which are unsafe for aerodynamic deceleration<sup>[27]</sup>. For this reason, a high-altitude velocity decrease maneuver must be carried out.

Given these considerations, including economic, programmatic, and physical constraints, a controlled propulsive landing has been selected as the re-entry strategy for the TERR-1 system. Detailed plots and further analysis supporting this decision are provided at the end of Section 6.3.3.

The main advantages of a controlled propulsive landing strategy are:

- Landing Precision: re-entry burns enable highly accurate landings, allowing TERR-1 first stage to be guided to specific zones on land or onto drone ships at sea.
- Controlled Descent: gradual deceleration provided by re-entry burns minimizes impact forces, preserving the structural integrity of the booster, crucial for reusability, turnaround time and cost.

The TERR-1 re-entry strategy comprises the following phases (hardware is expanded upon in Sections 6.3.2 and 10):

Phase	Description
a. Stage Separation	<ul style="list-style-type: none"> <li>• After the first stage burn out, it separates from the second stage using a pyrotechnic mechanism, which also imparts a small <math>\Delta v</math> to the booster, ensuring a safe clearance from the second stage, which continues carrying the payload into orbit.</li> </ul>
b. Coasting and Orientation	<ul style="list-style-type: none"> <li>• The booster coasts along a suborbital ballistic trajectory.</li> <li>• The booster performs a 180° flip maneuver using cold thrusters to orient itself in a tail-first configuration, positioning the engines toward the ground in preparation for the re-entry burn.</li> <li>• Grid fins are deployed to aerodynamically control the descent trajectory, ensuring stability.</li> </ul>
c. Re-entry burn	<ul style="list-style-type: none"> <li>• Some of the engines are re-ignited, creating a counter-thrust to perform a re-entry burn. This is necessary to reduce the heat flux, minimizing the velocity as the booster enters the denser layers of the atmosphere.</li> </ul>

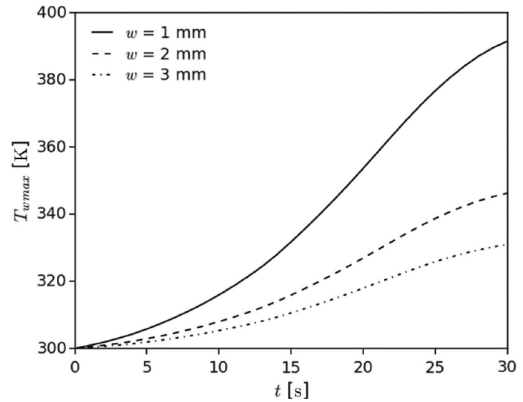
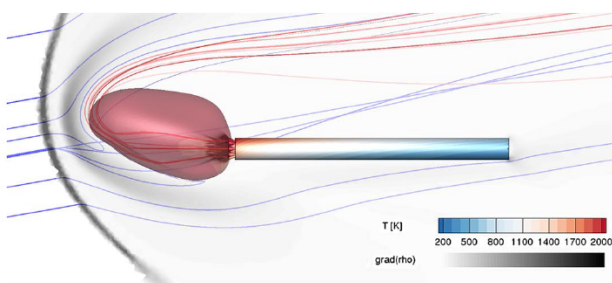
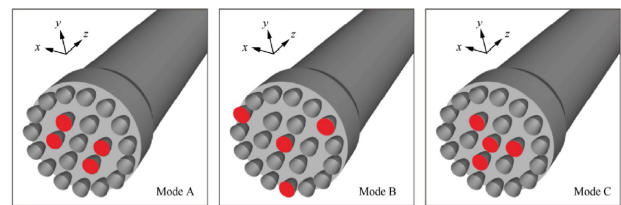
Phase	Description
d. Controlled aerodynamic descent	<ul style="list-style-type: none"> <li>In this unpowered phase, the booster remains in tail-first configuration and uses the grid fins to maintain stability while decelerating exploiting aerodynamic braking.</li> </ul>
e. Landing burn	<ul style="list-style-type: none"> <li>As the booster nears the landing zone, some of the engines are re-ignited for a landing burn which gradually slows the booster to a near-zero velocity at touchdown.</li> <li>Throttatable engines are needed to achieve precise control over the descent rate.</li> </ul>
f. Landing	<ul style="list-style-type: none"> <li>Retractable landing legs are deployed shortly before touchdown to absorb the landing impact and stabilize the vehicle.</li> </ul>

Table 13: Stages of Booster Descent and Recovery

### 6.3.1 Thermal Analysis of Hypersonic Retro-propulsion for Reusable Launch Vehicles

The re-entry strategy for this preliminary design is based on SpaceX's Falcon 9, which represents the most successful implementation of supersonic rocket retropropulsion for safe re-entry and vertical landing. A key focus of this analysis is the thermal loads on critical components, particularly the engine base, as the vehicle operates in a tail-first configuration during re-entry, with engine re-ignition being essential for mission success.

During retropropulsion, the first stage is partially submerged in the exhaust plume, which significantly influences the thermal environment. A numerical fluid dynamics study is used to evaluate plume-vehicle interactions based on Falcon 9 dimensions<sup>[28]</sup>. Results indicate that while gas temperatures in the plume are high, the low gas density results in manageable heat fluxes, causing only a moderate temperature increase on the cylindrical walls when using standard aluminum materials, such as Al-Lithium 2090-T83 used in the TERR-1 system (see Section 4.2.3), as shown in Figure 16. The extent of plume interaction varies with the trajectory position, from complete submersion of the vehicle to partial submersion of the base plate, leading to varying heat flux distributions. This variability must be accounted for when estimating structural heating during retropropulsion. Temperature contours at re-entry burn conditions are shown in Figure 17.

Figure 16: Maximum wall temperature over time for selected wall thicknesses<sup>[28]</sup>Figure 17: Temperature contours at re-entry burn conditions<sup>[28]</sup>Figure 18: Three types of retropropulsion modes<sup>[29]</sup>

An additional aerothermodynamics study<sup>[29]</sup> explored optimal multiple engine geometries for the re-entry burn. The configurations considered are shown in Figure 18.

Mode C, validated by Falcon 9, is identified as the most suitable for TERR-1, offering a balance between thermal and aerodynamic loads on the engine base and rocket walls. However, certain adaptations are required since, although the engine base geometry is similar to that adopted for TERR-1 (as discussed

in Section 3), the reference study<sup>[29]</sup> is based on a rocket with 22 engines, compared to the 18 engines on TERR-1. This configuration also adheres to the upper heat flux limit of  $200 \text{ kW/m}^2$ <sup>[27]</sup>, set for both ascent and descent trajectories as shown in Figure 19.

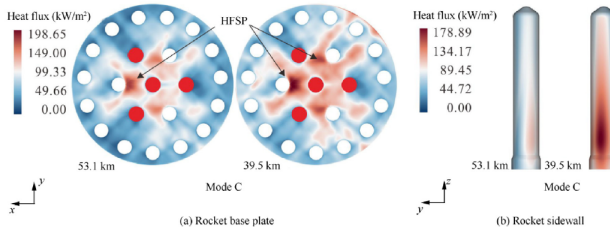


Figure 19: Rocket base plate and side wall heat flux distributions<sup>[29]</sup>

From this literature analysis, the key findings relevant to the TERR-1 system design are:

- **Engine Configuration:** A multi-engine configuration is preferred for the supersonic re-entry burn. This setup facilitates the formation of a stable Mach disk between the bow shock and the rocket, reducing vorticity and improving thermal and aerodynamic load distribution on both the engine base and rocket walls<sup>[29]</sup>.
- **Heat Flux Behavior:** As re-entry altitude decreases, the heat flux on the rocket base plate remains relatively constant and represents the most critical area requiring thermal isolation, whose design will be accounted for in a future development iteration, to ensure engine re-ignition. In contrast, the heat flux on the side walls increases significantly but remains manageable when using standard aluminum based materials without additional thermal protection<sup>[29][28]</sup>.

A more comprehensive study will be conducted in future design phases to refine the thermal environment assessment and ensure proper system implementation (see Section 10).

### 6.3.2 Re-entry and Landing hardware

**Grid Fins:** The TERR-1 launch system uses foldable grid fins for stabilization, deceleration, and trajectory control during re-entry and landing. These fins, along with thrust vector control and cold-gas thrusters, aid aerodynamic steering during descent. Various configurations are being considered (see Appendix E.3, Figure 35), with a detailed aerodynamic analysis needed later to identify the best option.

**Landing System:** The landing system's preliminary design is reverse-engineered from Falcon 9, featuring four rotating legs deploying just before touchdown. These legs, made from carbon fiber and an aluminum honeycomb core, have independent damping systems to absorb impact energy. Carbon fiber offers stiffness, while the aluminum core improves energy absorption due to its high deformability, protecting against impact forces. This concept will be refined in future design iterations to meet the specific requirements of the TERR-1 system.

### 6.3.3 Re-entry Trajectory Simulation

To assess the feasibility of a controlled retro-propulsion re-entry strategy for the TERR-1 system, a re-entry trajectory simulation is conducted using input data from all subsystems. The input data and initial conditions used for the re-entry trajectory simulation are summarized below:

T	448 380 N
$M_{S,1}$	1 487.24 kg
$M_{P,landing,1}$	764.84 kg
$d_1$	1.8 m
$A_{wet}$	$2.54 \text{ m}^2$
supersonic $C_D$	1.582
subsonic $C_D$	0.8

$$x_0 = \begin{bmatrix} v = 3.03 \text{ km/s} \\ \gamma = 26.61^\circ \\ r = R_\oplus + 96 \text{ km} \end{bmatrix}$$

Table 14: Input data

The equations of motion employed in this simulation are a simplified adaptation of those used in the ascent trajectory optimization (see Section 6.2.2). These equations have been modified to account for the limitations of the Round Earth Model in scenarios where the flight path angle approaches  $\pm 90^\circ$  and the velocity approaches zero, both critical conditions for the re-entry phase. The key modification involves implementing a switch logic in the dynamics. This logic activates when the flight path angle approaches  $-90^\circ$ , switching to a simplified set of equations where the flight path angle is kept constant. This decouples the flight path angle from the velocity, enabling accurate convergence to the target velocity of 0 m/s. In this simulation, the lift force and angle of attack are neglected to ensure consistency with the other subsystems. Furthermore, two constant drag coefficient values are used: one for the supersonic regime and another for the subsonic regime since no attitude change is considered throughout the descent.

A trial-and-error approach has been employed to tune the simulation parameters, which are: engine throttle settings, ignition altitudes, and burn durations, to meet the following landing targets<sup>[27]</sup>.

Landing Altitude	Landing Velocity	Flight Path Angle
0 m $\pm$ 10 m	0 – 2.5 m/s	$-90^\circ \pm 2^\circ$

Table 15: 1st Stage re-entry landing targets

These targets are achieved while remaining within the following constraints:

Consumed Propellant Mass	Dynamic Pressure	Heat Flux	Lateral Acceleration
$\leq$ re-entry propellant mass	< 200 kPa	< 200 kW/m <sup>2</sup>	< 3g

Table 16: 1st Stage re-entry constraints

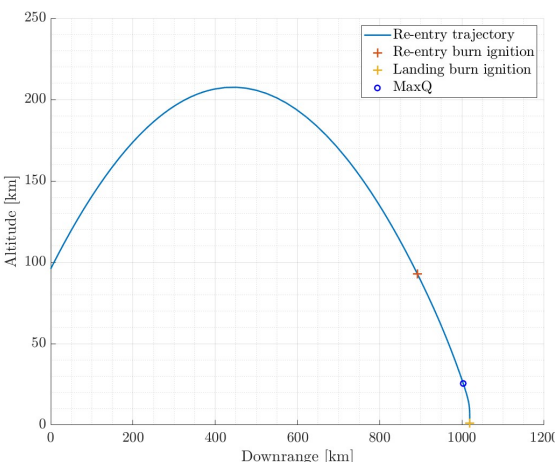
Regarding the re-entry propellant mass estimation, see Section 4.2.1. The trajectory-related constraints, such as dynamic pressure, heat flux, and maximum acceleration, are derived from reverse-engineered data from SpaceX Falcon 9 flights<sup>[27]</sup>.

The heat flux is estimated using the modified Chapman equation<sup>[27]</sup>:

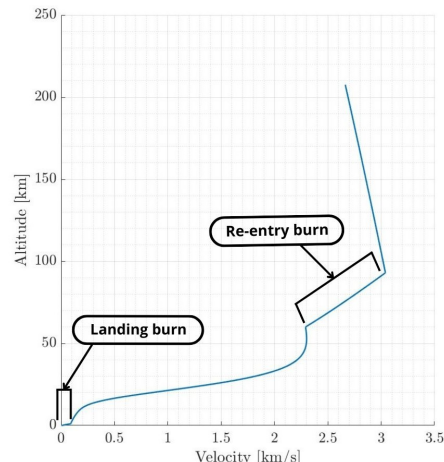
$$\dot{q} = 20\ 254.4 \text{ W/cm}^2 \sqrt{\frac{\rho}{\rho_R} \frac{R_{N,r}}{R_N}} \left( \frac{v}{v_r} \right)^{3.05} \quad (18)$$

where  $R_{N,r}$  is the reference nose radius (1 m),  $R_N$  is the vehicle nose radius (0.9 m for TERR-1),  $v$  is the vehicle velocity, and  $v_r$  is the reference velocity (10 000 m/s)<sup>[27]</sup>.

The resulting trajectory and velocity plots, including the re-entry and landing burns, are presented in Figure 20.



(a) Re-entry Trajectory



(b) Re-entry profile (Velocity over Altitude)

Figure 20: Results of 1st Stage re-entry

As illustrated, the booster follows a quasi ballistic trajectory, reaching a peak altitude of approximately 208 km at a velocity of 2.66 km/s. This high-altitude peak is expected considering the state at staging condition. During its descent, the booster continues on a ballistic path until it reaches an altitude of 93 km, where a re-entry burn is initiated. This burn lasts for 25 seconds (from 333 s to 358 s after stage separation) and is performed using four engines operating at 63% throttle. By the end of this burn, the booster's altitude and velocity are reduced to 60 km and 2.3 km/s, respectively.

Following the re-entry burn, the booster enters an unpowered free-fall phase, utilizing aerodynamic drag for braking. This phase continues until the booster descends to an altitude of 1 km, where a final landing burn is executed. During this burn, a single engine operates at 66 % throttle, reducing the booster's velocity to 2.4 m/s at touchdown. The time variations of velocity, altitude, flight path angle, downrange distance and tangential and lateral accelerations for the re-entry trajectory are shown in Appendix E.3, Figures 30, 31.

Regarding the constraints, as shown in Figure 21, the heat flux and dynamic pressure remain within acceptable limits throughout the trajectory, even during the most critical phase near  $\max q$ , which occurs at an altitude of approximately 25.5 km.

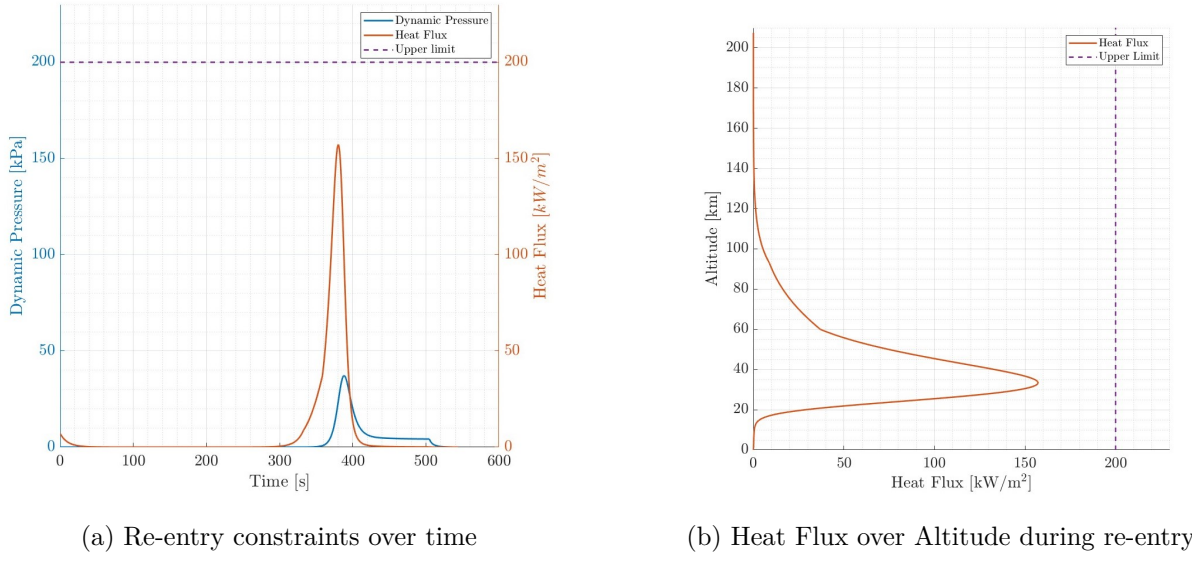


Figure 21: Heat flux and dynamic pressure profiles of first stage during re-entry

Furthermore, an initial simulation of the trajectory is conducted without any retro-propulsive maneuver to evaluate natural dynamics and consequently compare different re-entry strategies. This simulation demonstrated that a parachute-based re-entry approach would be unfeasible for the TERR-1 system. Specifically, the heat flux exceeds the system's upper limits (see Appendix E.3, Figure 34), and the Mach number reached (up to more than Mach 7, see Figure 33 in Appendix E.3) during descent and before the most critical thermal condition makes parachute deployment unfeasible<sup>[30]</sup>. Based on these findings, a velocity-reduction maneuver in the upper part of the atmosphere is essential to remain within the system's thermal and aerodynamic bounds. Consequently, a controlled retro-propulsive re-entry strategy is selected as the optimal approach for the TERR-1 design.

## 6.4 Re-entry of second stage

After analyzing the re-entry strategy for the first stage of the launcher, a further study is carried out to evaluate the deorbiting and the possibility to recover the second stage (TERR1-HLR-007). The initial conditions of the second stage upon reaching the nominal trajectory are:

$$x_0 = \begin{bmatrix} v = v_{Earth} + 7.6658 \text{ km/s} \\ \gamma = -0.5^\circ \\ r = R_\oplus + 403 \text{ km} \end{bmatrix}$$

As the second stage reaches orbital velocity, performing an accurate deorbit burn is essential to reduce

its speed to at least 7.56 km/s, ensuring atmospheric reentry (see Appendix E.4, Figure 36). For the TERR-1 second stage, this maneuver is a significant challenge as it requires a  $\Delta v$  that demands additional propellant. Although the vehicle achieves its nominal orbit at 403 km altitude with 0.15% of the propellant mass left, this allocation appears insufficient to provide the required  $\Delta v$  for deorbiting. While the primary mission requirement of payload delivery to the intended orbital altitude has been successfully met (TERR1-HLR-005), this situation highlights the need for further design refinements. A detailed analysis must account for the additional propellant required for the deorbit burn, a factor that would influence the vehicle's design.

Regarding the possibility of reusing the second stage, the primary concern is the survivability of the system through the extreme heat conditions met re-entering with orbital velocity<sup>[31]</sup>. Indeed, the most critical challenge lies in the extreme heat flux generated during re-entry. As shown in Figure 22, the heat flux begins to rise sharply below an altitude of 150 km, peaking at  $1054 \text{ kW/m}^2$  at 60 km. This value far exceeds the established limit of  $200 \text{ kW/m}^2$ <sup>[27]</sup> for the TERR-1 system, creating a critical thermal environment.

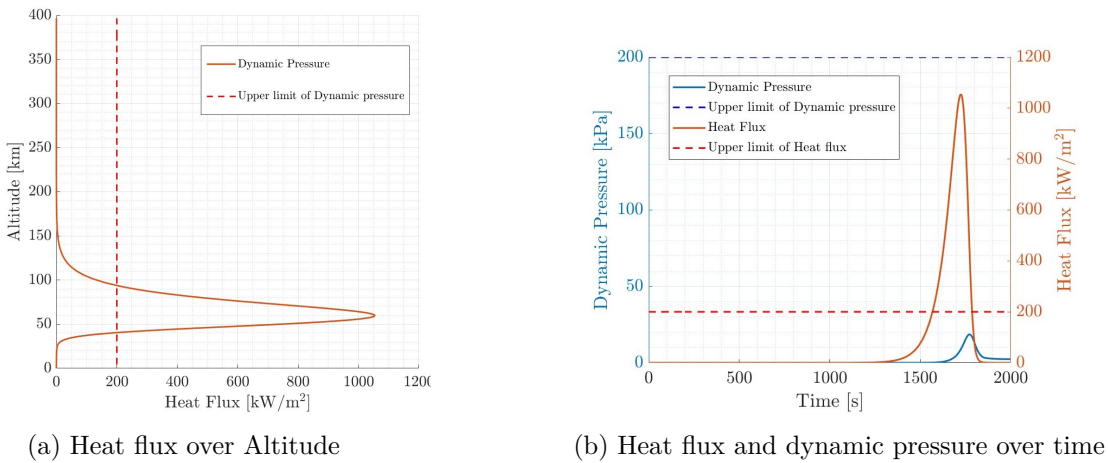


Figure 22: Heat flux and dynamic pressure values of re-entry of second stage

Developing a reusable second stage also presents other technological challenges. Adding recovery systems would require thorough testing and innovative design solutions, significantly increasing costs and extending development time. This process involves iterative design phases and extensive material testing, while addressing current constraints such as a tight time-to-market requirement (TERR1-HLR-009) and with recovery technologies not yet mature.

These considerations render the formulation of a feasible re-entry and recovery plan impractical for the second stage of the TERR-1 system.

## 7 Structures

A preliminary structural analysis is conducted in order to determine the loads upon interfaces. The results are then used to estimate thicknesses of each stage.

### 7.1 Discretization of Launcher

The launcher is segmented into 11 main components defined in Table 17 and shown in Figure 23.



Figure 23: 2D segmented schematic of launcher generated in OpenRocket with resultant dimensions

The reason behind the segment separation is to inspect the launcher part by part analyzing how much load they bear individually. Afterwards, thickness of each segment can be computed to withstand the most critical flight conditions. Since diameter of the structure are set after the discretisation, the lengths of hollow components can be obtained as shown from Eq. 24 to Eq. 29 in Appendix C.

<b>Number</b>	<b>Component</b>	<b>Number</b>	<b>Component</b>	<b>Number</b>	<b>Component</b>
1	Payload - Fairing	5	2nd Stage - RP-1 Tank	9	1st Stage - Inter-Tank
2	2nd Stage - Forward skirt	6	2nd Stage - Aft Skirt	10	1st Stage - RP-1 Tank
3	2nd Stage - LOX Tank	7	Interstage	11	1st Stage - Aft Skirt
4	2nd Stage - Inter-Tank	8	1st Stage - LOX Tank		

Table 17: Segmentation of the launcher

## 7.2 Internal Loads and Stresses

The load analysis treats each component as a 2D beam. The accounted forces are the inertial ones, drag and thrust while the lateral air loads are neglected. However, an initial hint of the last aforementioned loads can be obtained by the distributed pressure computed in the aerodynamic analysis. In order to compute the local forces, it is possible to analyze the reactions among the 11 different beams, therefore, the problem can be reshaped in matrix form:  $Ax = b$ , which is expanded in Appendix C.1.

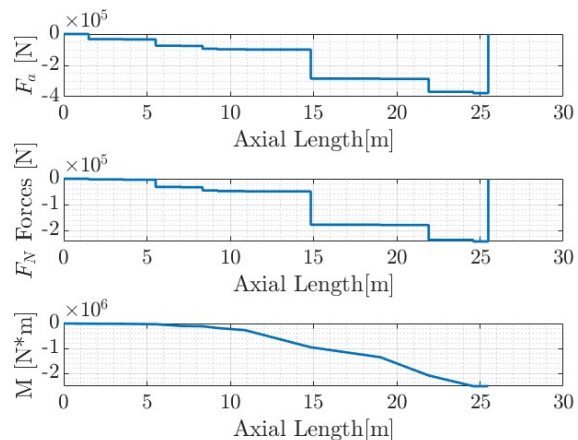
To avoid ambiguity, it is necessary to define a sign convention, chosen as follows: the axial direction is positive towards the nose while the radial direction is positive downward relative to the rocket axis.

The previously described model adapts its shape according to stages, thus to the involved modules. Nevertheless, a difference lies between the first two stages and the re-entry structural analysis. Indeed, in the TERR-1 case, the analysis of the loads starts at tip and terminates at the launcher bottom, while the opposite is done for the re-entry. Subsequently, the stress analysis is conducted as illustrated in the Appendix C.2.

Therefore, this method can be iterated along each flight regime and for the two stages, computing the minimum thickness for each of them. Therefore, a thickness matrix is obtained and it is possible to investigate and size each module accordingly to its most critical condition. Furthermore, the ground analysis for both transport and wind loads is neglected for simplicity. The propellant level in the tank and masses, which affect the internal loads, are evaluated according to the flight time knowing the flow rate.

### 7.2.1 Axial Forces, Shear and Bending Moment

Once obtained the internal reactions, it is possible to compute the loads per component. In particular, as expected, the shear and the axial loads are equal to the magnitude of the thrust in their respective directions. The bending moment does not converge to zero; indeed, a torque is imposed by the engine to have a favorable  $\dot{\gamma}$ . Similarly, the rotational inertial forces are neglected here and can be further investigated in a more advanced analysis. Finally, the thickness computation can be carried out, and, consistently with the theory, the most compelling condition occurs at  $\max q$  during the initial flight phases for all launcher modules (see Figure 24). This result is reasonable for the second-stage modules as well, since, even though they undergo higher acceleration at higher altitudes (see Figure 15a), the external applied forces and inertial loads are considerably lower. Similarly, for the first stage, the most constraining load condition occurs during the initial engine ignition, despite the structure experiencing its highest acceleration during re-entry.

Figure 24: Axial Forces, Shear Forces, and Torque at  $\max q$ 

Similarly, for the first stage, the most constraining load condition occurs during the initial engine ignition, despite the structure experiencing its highest acceleration during re-entry.

### 7.3 Final Structure

The final dimensions of the launcher are tabulated below:

Component	Length (m)	Thickness (mm)	Diameter (m)	Sub-Component Within
Payload Fairing (1)	3.60	0.96 (1)		Payload
2nd Stage Forward Skirt (2)	1.50	1.11 (1.15)		Avionics
2nd Stage LOX Tank (3)	0.84	1.12 (1.15)		Insulation
2nd Stage Inter-Tank (4)	2.25	1.14 (1.15)		Pump
2nd Stage RP-1 Tank (5)	0.29	1.12 (1.15)		-
2nd Stage Aft Skirt (6)	1.50	1.18 (1.20)	1.80	Thrust Structure, Engine, Gimbal
Interstage (7)	1.80	2.10 (2.10)		Avionics
1st Stage LOX Tank (8)	6.11	3.39 (3.40)		Insulation
1st Stage Inter-Tank (9)	2.25	3.89 (3.90)		Pump
1st Stage RP-1 Tank (10)	3.56	4.61 (4.65)		-
1st Stage Aft Skirt (11)	1.80	4.93 (4.95)		Thrust Structure, Engine, Gimbal

Table 18: Dimensions and sub-components within the discretized main modules

The values in parenthesis are rounded up for manufacturing.

### 7.4 Boeing 747-400 structural verification

The selected carrier is the Boeing 747-400 and the main parameters are reported below:

Launcher Mass [kg]	Engine Mass [kg]	Fuel Mass [kg]
34 797.62	4 386	30 000
Aircraft Mass [kg]	MTOW [kg]	b [m]
184 567	396 894	29.21

Table 19: Masses of the airplane

For the selected carrier aircraft, the launcher is installed beneath the wing through an adapted engine attachment pylon. The objective of the feasibility verification is to determine whether the wing is capable of withstanding the maximum shear forces and bending moments at its root while accommodating the launcher. To evaluate this feasibility, a reverse-engineering approach is used to retrieve the limit loads. In accordance with CS-25 EASA certification standards<sup>[32]</sup> for large commercial aircraft, the maximum load factor for normal flight is  $n_{max} = 2.5$  and for inverted flight is  $n_{max} = -1$ . The operational conditions analyzed in this study involve upward bending, caused by aerodynamic lift, and downward bending, resulting from the weight of the launcher during ground operations such as taxiing. The analysis assesses the structural limitations of the wing under these primary loading conditions to ensure its integrity and suitability to carry the launcher. To meet the certification standard, a commercial airplane must operate within this maneuvering envelope. To compute the maximum shear and moment at the root, as first approximation, a constant distribution of lift is assumed. In the computation, the fuel and engines masses are also taken into account. From the load factor definition:

$$L_{max} = \frac{MTOW}{2} n_{max} g \quad (19)$$

where  $L_{max}$  represents the lift generated by the semi-span wing. The specified boundaries for both upward and downward bending are as follows: for downward bending, we have  $T_{max} = 1.37 \cdot 10^6 N$  and  $M_{max} = 2.014 \cdot 10^7 Nm$ . In contrast, for upward bending, the limits are  $T_{max} = -3.4255 \cdot 10^6 N$  and  $M_{max} = -5.0356 \cdot 10^7 Nm$ . The results of the downward bending condition considering a fuel mass of  $M_{fu} = 100 000 kg$  are presented below. This scenario is identified as the critical condition due to the combined weight of the fuel, engines, and the launcher. Consequently, this imposes a constraint on the fuel mass, which affects the operational flight duration. The time required for the operations of the carrier aircraft can be assumed less than three hours<sup>[22]</sup>, resulting in  $M_{fu} = 30 000 kg$ , therefore a similar operational time is assumed.

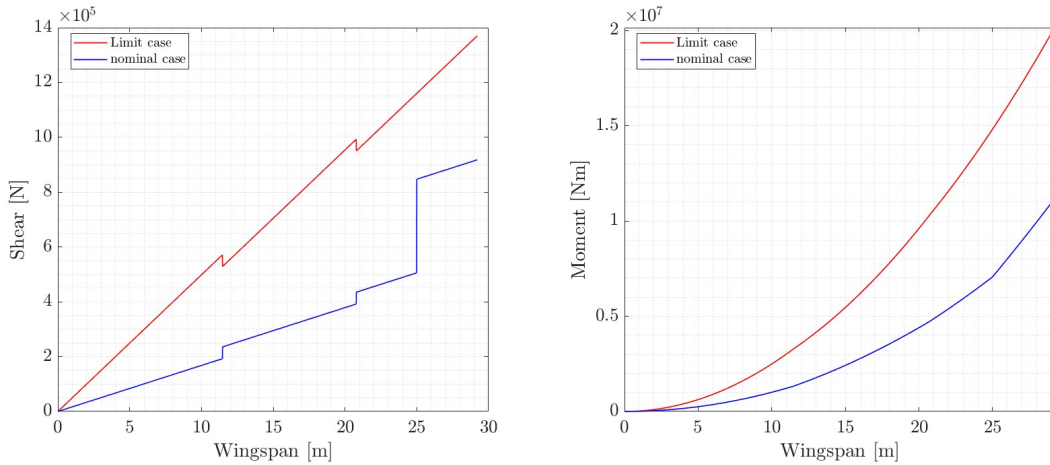


Figure 25: Downward shear force and bending moment

Figure 25 illustrates the shear and moment evolution starting from the wing tip, posed at the center of the reference frame, up to the wing root, where maximum stresses are expected. The loads consist of a uniform fuel distribution, concentrated loads from the engines and the launcher. During take-off, with an assumed load factor of  $n = 1.2$  a uniform lift distribution is included in the load calculations. This condition is not critical since the weight of the LV reduces the maximum loads at the root. All the previous assumptions are deemed reasonable for a first iteration of project. This approach confirms the suitability of the chosen carrier. Literature analysis has been carried out to ensure that the mechanic link between wing and launcher can withstand the weight of the LV<sup>[2]</sup>.

## 8 Monte Carlo Analysis

A Monte Carlo simulation has been employed to assess the project accuracy (see Figure 26). Within this framework, some input variables are modeled as stochastic, incorporating random uncertainties according to a normal distribution, while others are classified as epistemic and are modeled with a uniform distribution. The analyzed stochastic variables include the specific impulse, the payload mass, the thrust, the diameter and length of each component. The epistemic variables are the density of fuel and oxidizer. These parameters have been chosen due to their crucial role to both the launcher and mission profile. The standard deviation introduced for the payload mass is  $\sigma_{pay} = 1 \text{ kg}$ , for the thrust is  $\sigma_T = 100 \text{ N}$ , and the specific impulse is  $\sigma_{I_{sp}} = 3 \text{ s}$ . For the geometrical parameters, the variance on the diameter is  $D = 3 \text{ mm}$  and on the length is  $L = 3 \text{ mm}$ . Subsequently, the masses are determined using these geometrical parameters, by summing all the components.

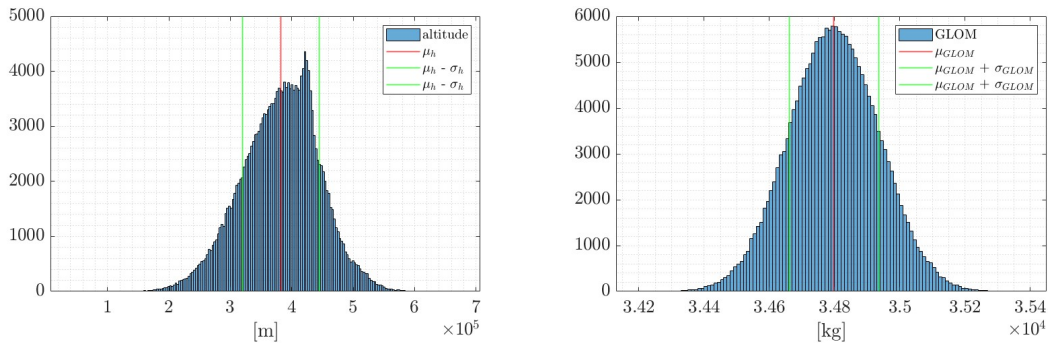


Figure 26: Histogram of altitude and GLOM

In this simulation, 200 000 iterations are conducted. The values for the mean and standard deviation have converged, as indicated by a relative error of less than 1% as shown in Appendix F. From the simulation, GLOM and orbit altitude are analyzed with respect to both their mean and standard deviation, and their results are presented below:

Parameter	Mean	Standard Deviation
GLOM [kg]	34 797.96	137.4
Orbit Altitude [km]	381.880	62.645

Table 20: Results Summary

The results from the GLOM align very closely with the nominal value (Table 7). In contrast, the Monte Carlo simulation demonstrates that the orbital accuracy is not achieved in terms of both the mean value and standard deviation. This result is expected, as the trajectory does not incorporate any control system.

## 9 Costs analysis and Return On Investment (ROI)

The high level requirement TERR1-HLR-006 (Table 1) defines that the Return on Investment (ROI) shall be achievable with a limited number of reuses of the launcher. The ROI is an index that measures the efficiency of an investment and it is calculated using the following formula:

$$ROI \% = \frac{revenue - cost\ per\ flight}{cost\ per\ flight} \cdot 100 \quad (20)$$

The Cost per Flight ( $CpF$ ) is derived using a parametric model<sup>[33]</sup>, which integrates the T1 Equivalents method, commonly employed by space agencies, and the three-part estimate methodology (see procedure in Appendix G)<sup>[34]</sup>.

The cost analysis and ROI computation have also been performed for an expendable launch vehicle (*ELV*) to highlight the economic benefits of using a reusable launch vehicle (*RLV*). As shown in Figure 27 (left), the  $CpF$  for an *RLV* is significantly lower than that of an *ELV*, demonstrating that reusability reduces production costs. For the computation of the ROI (Figure 27, middle), the same amount of investment has been assumed equal to the first  $CpF$  of the *RLV* and the margin on the profit is 8%<sup>[33]</sup> of the  $CpF$  for both *RLV* and *ELV*. Whereas, in Figure 27 (right) the margin on the profit of the *ELV* profit is 4% lower than the *RLV* one, assuming a minor number of customers due to the higher  $CpF$ . It can be seen that in the hypothesis of the same profit amount, the ROI results to be more faster for an *ELV*, while the ROI is faster in case of having an higher profit in the reusable case.

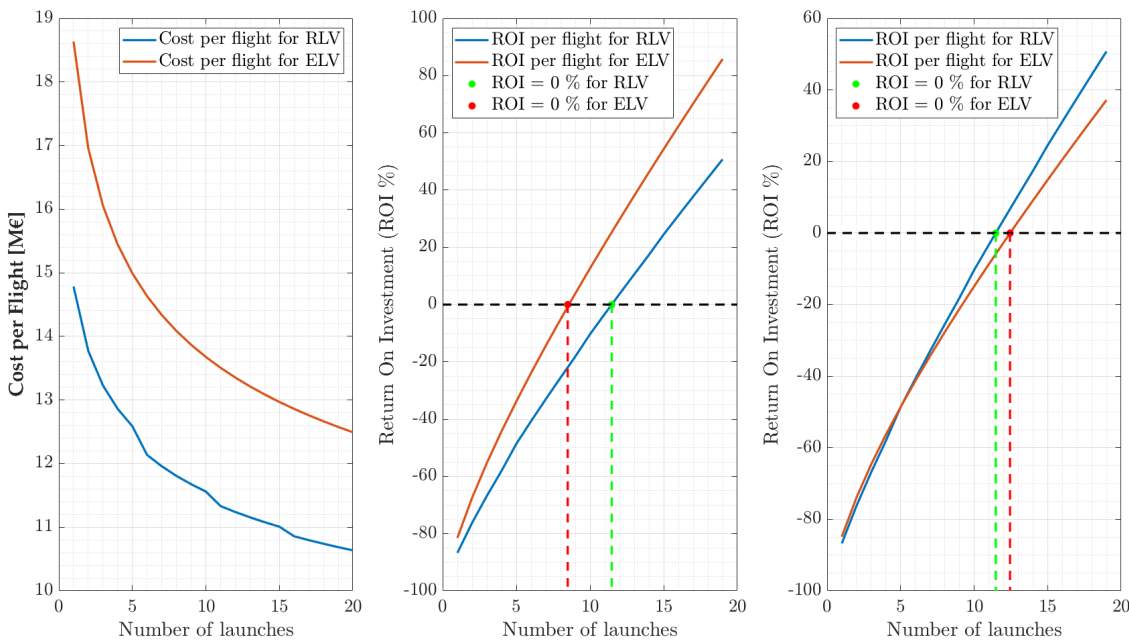


Figure 27: Results of the cost analysis and ROI computation

To validate the optimization of the Expendable Mass model, previously described in Section 4, an

additional cost analysis is conducted using the mass values derived from this method, comparing them with the results obtained with the GLOM optimization and the ones obtained for ELV. The model accuracy is confirmed by the data presented in Table 21, where the cost items resulting from the optimization of the Expendable Mass are generally lower than those of the *ELV* and those from the GLOM optimization. It is important to note that the largest cost difference between the *RLV* and *ELV* lies in the manufacturing costs, as anticipated. This is due to the fact that the components of the first stage are produced every five launches for the *RLV*.

	<b>Reusable Launch Vehicle</b>	<b>Expendable Launch Vehicle</b>	<b>Optimization of Expendable Mass</b>
Development costs [M€]	86	86	85
Manufacturing costs [M€]	9.58	17	9.4
Operations costs [M€]	0.97	0.98	0.98
Cost per Flight [M€]	14.7	18.6	14.5

Table 21: Main cost items of the launcher

## 10 Conclusions and Future Improvements

This project aims to evaluate the feasibility of developing a launcher capable of delivering a 250 kg payload to a Sun-Synchronous Orbit (SSO) in a tandem configuration. The first iteration of the preliminary design for the main subsystems has been completed. The design has been guided by the defined requirements and shows promising results that warrant further exploration in future iterations. In particular, as shown in the Table 22, all mandatory requirements have been met. However, the requirement for the recoverability of the second stage could not be achieved due to technical constraints, and the "short time to market" requirement needs further investigation in subsequent iterations.

REQ. ID	IMPORTANCE	REQUIREMENT	RESULT	COMMENT	FUTURE STEPS
TERR1-HLR-001	M	SAFE LAUNCH	✓	-	Study and model: - Stage Separation - Carrier and fairing separation
TERR1-HLR-002	M	RECOVERABILITY OF THE FIRST STAGE	✓	Possible but complex	Model: - Implement precise control system - Perform deeper heat analysis
TERR1-HLR-003	M	TANDEM CONFIGURATION	✓	-	- Decrease the diameter
TERR1-HLR-004	M	LAUNCH FROM CIVIL AIRCRAFT	✓	-	Check flight dynamic of the carrier
TERR1-HLR-005	M	TARGET ORBIT	✓	-	Model the complete dynamic of the trajectory
TERR1-HLR-006	M	SMALL NUMBER OF REUSES FOR ROI	✓	Possible	Improve the business model
TERR1-HLR-007	NH	RECOVERABILITY OF UPPER STAGES	✗	- Low TRL : Impossible in 4 years - Not enough propellant to deorbit - Needs of complex TPS	Study disposal of upper stage according to SpaceDebris Regulation
TERR1-HLR-008	NH	TOXICITY OF PROPELLANT	✓	RP1-LOX is considered non toxic	Evaluate modern CH4-LOX engines
TERR1-HLR-009	NH	SHORT TIME TO MARKET	-	Possible, but re-entry could delay operations	Re-evaluate when more design details are known

Table 22: Mission Requirements Verification in the First Iteration

Before moving on to the final considerations, it is important to review each subsystem individually to assess the current status. In particular, this involves highlighting the challenges to be addressed in future iterations and emphasizing the strengths of the work accomplished so far.

**MISSION ANALYSIS:** The  $\Delta v$  budget can be more accurately estimated, particularly regarding losses, by incorporating the outputs obtained from subsystems in the first iteration, such as aerodynamics and trajectory. Additionally, the carrier's analysis can be further refined in terms of launch altitude, flight path angle, and initial launcher velocity.

**PROPELLION:** This preliminary propulsion subsystem design has been developed under several assumptions due to lack of official information. Consequently, it is reasonable to expect that the design could be further refined by accessing detailed datasheets from Rocket Lab, as well as acquiring

the engine to conduct a testing campaign for the integration in TERR-1 system. Furthermore, a more accurate thrust profile model can be developed to account for variations in thrust with altitude. Additionally, the initial thrust at the start of the flight can be calculated with greater precision based on the newly selected expansion ratio. Considering the integrated electric turbopump system, it is also necessary to account for the required power supply.

**MASSES:** The GLOM is higher in comparison to that of LauncherOne, however, having designed a reusable first stage for TERR-1, this is expected. A brief trial has been conducted using a smaller diameter and composite materials, achieving a GLOM of approximately 20 000 kg, that shows potential for future improvements, such as the selection of the expendable mass strategy, which may contribute substantial value to the project as a whole, also in economic terms. Concerning the results included in this report, the assessment is positive, as the launcher can endure the loads during all flight phases, it is compatible with the chosen aircraft, and more importantly, the outcomes demonstrate a perfect alignment between the two approaches used to compute masses. This is crucial because even a slight mismatch of a few kilograms can affect the payload capacity, leading to either an overestimation or underestimation of the performance. Furthermore, in the next steps additional mass should be considered to perform a proper detachment during the staging and to take into account additional structural components that for the moment have been neglected, such as landing legs, grid fins, cold gas thrusters and tanks, and aerodynamics fins. Finally, following the load analysis, the computed masses via MERs exceed the minimal requirement for sustaining the loads. Consequently, the current design overestimates the masses by approximately 1.13%.

**AERODYNAMICS:** To address aerodynamic instability, a closed-loop control system needs to be implemented, potentially combining thrust vector control (TVC), in conjunction with the Trajectory subsystem, with aerodynamic surfaces. Deflective fins can effectively reduce the workload on the thrust system and are highly efficient in conditions of elevated dynamic pressure. However, thermal and structural constraints must be taken into account. Bow-tie fin configurations can be considered due to their reduced drag and minimized size compared to the traditional delta configuration. Additionally, advanced materials, such as ceramic matrix composites, should be considered to meet thermal and structural requirements. Moreover, the aerodynamic model should be extended to a launcher with different cross sectional areas.

**TRAJECTORY:** A major source of uncertainty at this stage is the trajectory model, which requires comprehensive revision and increased complexity. Developing a 6-degree-of-freedom dynamics model, a control system, and incorporating the angle of attack are essential. A lift model can allow a earlier staging phase, reducing the first stage burning time, thus reducing the launcher GLOM. A lower staging altitude opens the possibility of parachute re-entry. A well-designed trajectory is the key to verifying the functionality of other subsystems. In particular, the initial pitch-up phase has proven to be the most delicate stage in this preliminary analysis, despite significant simplifications in the model. This phase requires a more detailed investigation, considering potential additional aerodynamic appendages. Additionally, a comprehensive simulation and detailed testing of the carrier aircraft evasive maneuver during launcher release are essential to validate the feasibility of this operation. These analyses will ensure the aircraft can achieve the required initial launch conditions while maintaining safety.

## RE-ENTRY AND RECOVERY:

- Stage 1: this preliminary study on the feasibility of a controlled propulsive re-entry strategy for the TERR-1 launch system indicates that such an approach could be successfully developed and integrated. Key areas for future development include implementing a 3D rigid body model to simulate the flip maneuver and attitude control, ensuring that external disturbances are effectively accounted for. Additionally, an optimization process should be incorporated to design the nominal re-entry trajectory. To ensure accurate navigation during re-entry, the implementation of a closed-loop onboard navigation and control system will be essential. A tailored thermal analysis model is also needed to assess the thermal conditions of the booster at various atti-

tudes and flight phases, allowing for more precise thermal protection strategies. Furthermore, specialized re-entry and landing hardware, such as pyrotechnic mechanisms for staging, cold gas thrusters for attitude control, grid fins, and landing legs, must be designed and integrated to meet the specific needs of the TERR-1 system. Furthermore, the design of infrastructure for landing and post-flight operations will be critical to facilitate recovery and ensure the reusability of the system. In future iterations, if the first stage is separated at reduced altitude and velocity, a parachute-based re-entry strategy could be explored. This approach would lower development costs and enhance the ROI.

- Stage 2: in this first iteration, stage 2 lacks sufficient propellant to provide the necessary  $\Delta v$  to perform deorbit maneuver and atmospheric re-entry. This issue can be addressed in future iterations by allocating some propellant mass specifically for deorbiting in the optimization algorithms. To ensure a precise and safe landing, a detailed trajectory simulation integrated with mission analysis will be essential to accurately determine the optimal deorbit point. Additionally, conducting a more comprehensive and precise analysis of the thermal environment during atmospheric re-entry is crucial to assess whether the stage will burn up entirely due to atmospheric friction. This analysis would provide valuable insights into heat flux, material behavior and the structural integrity of stage 2. It would also support the development of more effective debris management strategies, ensuring compliance with mitigation guidelines.

**STRUCTURE:** in future iterations, a more comprehensive analysis should be conducted, going beyond the limitations of a beam analysis and expanding the scope to account for a wider range of acting forces and the use of composite materials. Furthermore, the choice of grid density must carefully consider the varying load conditions encountered along the launcher.

**ECONOMIC VIABILITY:** the real challenge for this project lies in its economic feasibility. While the ROI is positive, the estimated launch cost in this iteration is approximately 41 000 €/kg of payload. This is far too high compared to competitors in the same market segment, who charge 25 000 €/kg or less. SpaceX, for example, offers rideshare services for CubeSats in SSO at approximately 6 000 €/kg<sup>[35]</sup>. Considering that the project is expected to enter the market in four years, the trend of decreasing launch costs will likely continue. To remain competitive, the cost per kilogram must drop to around 10 000–15 000 €/kg, which implies a total launch cost between €4 million and €6 million. A situation that is currently difficult to achieve despite the mass reductions discussed earlier. However a more precise business model should be implemented for future iterations to asses this matter.

In conclusion, this preliminary design proves that the project is feasible from an engineering perspective. While some technical issues require further refinement and exploration, the project is not economically sustainable at this time. It is necessary to revisit some customer requirements to lower launch costs or develop viable alternatives targeting a specific market segment. For the project to succeed, it must offer something innovative that appeals to the public, stakeholders, and the market while maintaining reliability. Airborne launchers have a nice appeal but are unlikely to dominate the market unless they introduce game-changing innovations.

## References

- [1] Dresia K. et al. "Multidisciplinary Design Optimization of Reusable Launch Vehicles for Different Propellants and Objectives". In: *Journal of Spacecraft and Rockets* (2021).
- [2] *LauncherOne Air-Launched Rocket*. 2018. URL: <https://www.airport-technology.com/projects/launcherone-air-launched-rocket/?cf-view&cf-closed>.
- [3] Virgin Orbit. *Virgin Orbit Operations from Spaceport Cornwall*. URL: <https://airspacechange.caa.co.uk/documents/download/4364>.
- [4] Robert A. Braeunig. *Basics of Space Flight: Rocket Propellants*. URL: <http://www.braeunig.us/space/propel.htm>.
- [5] Joseph Magee et al. *Thermophysical Properties Measurements and Models for Rocket Propellant RP-1: Phase I*. 2007. URL: <https://nvlpubs.nist.gov/nistpubs/Legacy/IR/nistir6646.pdf>.
- [6] Wessel Wessels. *Using RP-1 As Rocket Fuel – Advantages and Disadvantages*. URL: <https://headedforspace.com/using-rp1-as-rocket-fuel/>.
- [7] George P. Sutton and Oscar Biblarz. *Rocket propulsion elements*. John Wiley and Sons, 2017.
- [8] Don Eldberg and Willie Costa. *Design of Rockets and Space Launch Vehicles*. AIAA EDUCATION SERIES, 2022.
- [9] Rocket Lab. *Electron Payload User Guide*. <https://www.rocketlabusa.com/assets/Uploads/Electron-Payload-User-Guide-7.0.pdf>. 2022.
- [10] SITAEL S.p.A. *S-200 Scaled Microsatellite Platform - Datasheet*. Product Sheet. Mola di Bari, Italy: SITAEL S.p.A, 2015. URL: <http://www.sitael.com>.
- [11] eoPortal. *CALIPSO: Cloud-Aerosol Lidar and Infrared Pathfinder Satellite Observations*. Accessed: 2024-12-11. 2024. URL: <https://www.eoportal.org/satellite-missions/calipso#calipso-cloud-aerosol-lidar-and-infrared-pathfinder-satellite-observations>.
- [12] eoPortal. *CAS500 Satellite Mission*. Accessed: 2024-12-11. 2024. URL: <https://www.eoportal.org/satellite-missions/cas500>.
- [13] eoPortal. *HISUI Mission Planning*. Accessed: 2024-12-11. 2023. URL: <https://www.eoportal.org/satellite-missions/iss-hisui#hisui-mission-planning>.
- [14] eoPortal. *KOMPSAT-3*. Accessed: 2024-12-11. 2024. URL: <https://www.eoportal.org/satellite-missions/kompsat-3>.
- [15] eoPortal. *RADARSAT-2 Spacecraft*. Accessed: 2024-12-11. 2023. URL: <https://www.eoportal.org/satellite-missions/radarsat-2#spacecraft>.
- [16] eoPortal. *SLATS Mission Overview*. Accessed: 2024-12-11. 2023. URL: <https://www.eoportal.org/satellite-missions/slats#overview>.
- [17] F. Sabetta. *Gasdinamica*. Università La Sapienza, 2009.
- [18] Leland H. Jorgensen. "Prediction Of Static Aerodynamic Characteristics For Space-shuttle-like And Other Bodies At Angles Of Attack From 0 ° To 180°". In: *National aeronautics and Space administration* (1973).
- [19] Mancini Lucandrea. "Multi-disciplinary design and multi-objective optimization of solid- and liquid- rocket based launch vehicles". MA thesis. Sapienza University of Rome, Department of Mechanical and Aerospace Engineering, 2023.
- [20] Eugene Fleeman. *Tactical Missile Design*. American Institute of Aeronautics and Astronautics, 2019.
- [21] N.F. Krasnov. *Aerodynamics of Bodies of Revolution*. American Elsevier Publishing Company, 1970.
- [22] Virgin Orbit. *LauncherOne Service Guide*. <https://newspaceeconomy.ca/wp-content/uploads/2022/06/launcherone-service-guide-august-2020.pdf>. 2020.

- [23] P.M. Sforza. *Manned Spacecraft Design Principles*. Elsevier Science & Technology Books, 2015.
- [24] J.R. Wertz. *Spacecraft Attitude Determination and Control*. Springer Netherlands, 1978.
- [25] G. Di Campli Bayard de Volo. “Vega Launchers’ Trajectory Optimization Using a Pseudospectral Transcription”. In: 2019. DOI: [10.13009/EUCASS2019-0710](https://doi.org/10.13009/EUCASS2019-0710). URL: <https://www.eucass.eu/doi/EUCASS2019-0710.pdf>.
- [26] Northrop Grumman Corporation. *Pegasus Payload User’s Guide*. 2020.
- [27] Jascha Wilken et Sven Stappert. “Comparative analysis of European vertical landing reusable first stage concepts”. In: *CEAS Space Journal* (2024).
- [28] Tobias Ecker et Sebastian Karl Etienne Dumont et Sven Stappert et Daniel Krause. “Numerical Study on the Thermal Loads During a Supersonic Rocket Retropropulsion Maneuver”. In: *Journal of Spacecraft and Rockets* (2020).
- [29] Yifei SU et Peijie SUN et Yangwen CUI et Guigao LE. “Re-entry rocket basic flow characteristics and thermal environment of different retro-propulsion modes”. In: *CEAS Space Journal* (2024).
- [30] Stefania Carlotti. “Parachutes for re-entry”. In: *Launch Systems course* (2024).
- [31] Förste Sophie and Fasoulas Stefanos. “Analysis of Novel Concepts for the Return of Upper Rocket Stages”. In: *CAerospace Europe Conference* (2023).
- [32] EASA. *Certification Specifications for Large Aeroplanes*. European Aviation Safety Agency, Amendment 4 2007.
- [33] Curran R. Drenthe N.T. Zandbergen B.T.C. and Van Pelt M.O. “Cost estimating of commercial smallsat launch vehicles”. In: *Acta Astronautica* (2018).
- [34] Koelle Dietrich E. *Handbook of Cost Engineering and Design of Space Transportation Systems*. Ottobrunn Germany, 2013.
- [35] SpaceX. *Rideshare*. <https://www.spacex.com/rideshare/>.
- [36] James.S.Barrowman. “The practical calculation of the aerodynamic characteristics of slender finned vehicle”. In: *Catholic University of America* (1967).
- [37] Ariane Space. *Vega, User’s Manual*. 2014.
- [38] Erdem Dinçer. “Aerodynamic design and performance analyses of grid fin in supersonic flow using design of experiments and computational fluid dynamics”. In: *Graduate school of natural and applied sciences of Middle East Technical University* (2022).

## A Appendix A: House of Quality

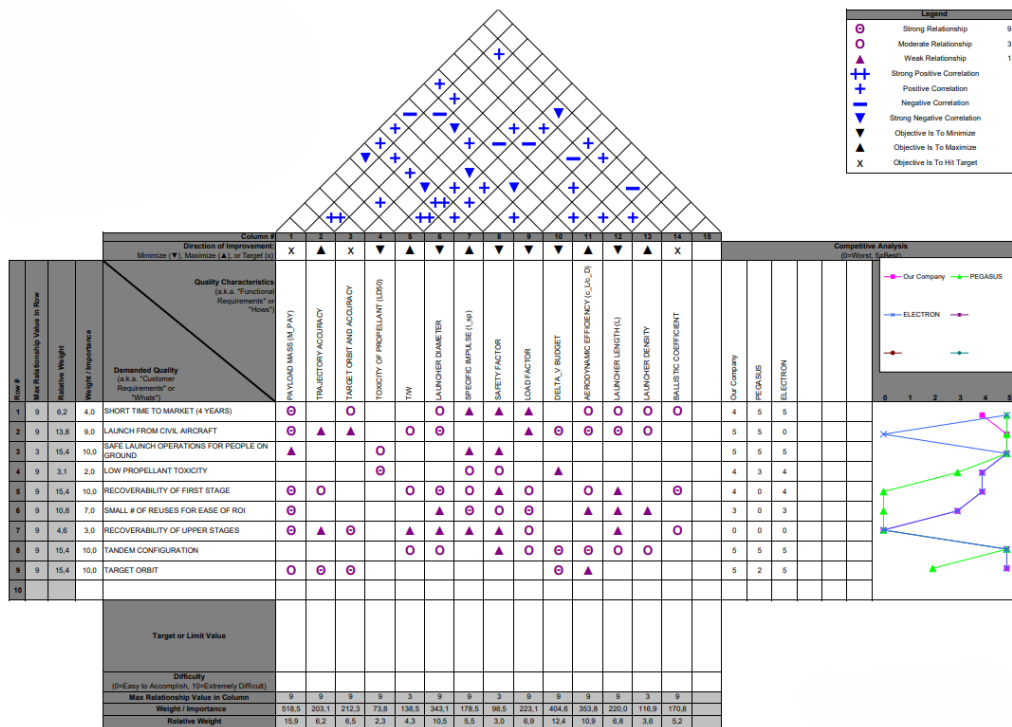


Figure 28: House of Quality

## B Appendix B: Propulsion

Engine	Thrust, kN		$\eta_p$ , s		$P_c$ MPa	$f$	$A/A^*$	Geometry		Ox/Fuel	Cycle
	SL	Vac	SL	Vac				L, m	D, m		
MA-5A Sust	269	378	220	309	5.07	2.27	25:1	2.46	1.22	LOx/RP-1	Gas gen
MA-5A Boost	1,910	2,104	265	296	4.96	2.25	8:1	2.57	1.22	LOx/RP-1	Gas gen
RS-27A	890	1,054	255	302	4.83	2.25	12:1	3.78	1.44	LOx/RP-1	Gas gen
RD-170	7,255	1,909	307	337	24.13	2.6	36:1	4.01	1.45	LOx/RP-1	Staged
RD-180	3,827	4,150	311	338	25.51	2.72	36.8:1	3.58	1.45	LOx/RP-1	Staged
Merlin 1V	N/A	411	N/A	342	N/A	N/A	N/A	N/A	N/A	LOx/RP-1	Gas gen
Merlin 1A	319	N/A	270	300	N/A	N/A	N/A	N/A	N/A	LOx/RP-1	Gas Gen
Merlin 1C	614.7	N/A	275	304	N/A	N/A	N/A	N/A	N/A	LOx/RP-1	Gas gen
LR87-AJ-11	1,984	2,353	254	302	5.70	2	15:1	3.84	1.50	N <sub>2</sub> O <sub>4</sub> /A-50	Gas gen
LR91-AJ-11	N/A	445	N/A	314	5.70	1.86	49.2:1	2.79	1.63	N <sub>2</sub> O <sub>4</sub> /A-50	Gas gen
RD-253	1,472	1,637	285	316	14.70	2.67	26.2:1	2.72	1.43	N <sub>2</sub> O <sub>4</sub> /UDMH	Staged
RD-0210	N/A	588	N/A	327	14.69	2.65	78.2:1	2.30	1.46	N <sub>2</sub> O <sub>4</sub> /UDMH	Staged
HM-60	885	1,140	334	431	11.00	5.3	45:1	2.87	1.75	LOx/LH <sub>2</sub>	Gas gen
RL10A-4-1	N/A	99.2	N/A	451	4.21	5.5	84:1	1.78	1.17	LOx/LH <sub>2</sub>	Expander
RL10B-2	N/A	110.3	N/A	467	4.44	6.0	285:1	3.05	2.14	LOx/LH <sub>2</sub>	Expander
RS-68	2,891	N/A	365	410	9.72	6.0	12.5:1	N/A	N/A	LOx/LH <sub>2</sub>	Gas gen
SSME 109%	1,818	2,279	380	453	22.48	6.0	77.5:1	4.27	2.44	LOx/LH <sub>2</sub>	Staged

Figure 29: Performance Characteristics of Selected Liquid-propellant Engines<sup>[8]</sup>

$$T_{\text{height}} = T_0 - T_{\text{grad}} \cdot h \quad \text{with } T_{\text{grad}} = 0.0065 \text{ K/m} \quad (21)$$

$$P_{atm,h} = P_0 \cdot \left( \frac{T_{\text{height}}}{T_0} \right)^{\frac{g_0 \cdot M_{mol}}{R_0 \cdot T_{\text{grad}}}} \quad (22)$$

$$\epsilon = \left\{ \left( \frac{k+1}{2} \right)^{\frac{1}{k-1}} \left( \frac{P_e}{P_c} \right)^{\frac{1}{k}} \sqrt{\left( \frac{k+1}{k-1} \right) \left[ 1 - \frac{P_e}{P_c} \right]^{\frac{k-1}{k}}} \right\}^{-1} \quad (23)$$

## C Appendix C: Masses and Structures

	Ullage	Shrinkage	Uncertainties	Total
Margin	3%	1.43%	2%	6.43%

Table 23: Margins for tank volumes<sup>[8]</sup>

$$h_2 = \frac{1}{3}d + h_{dome,2} \quad (24)$$

$$h_4 = \frac{1}{4}d + 2h_{dome,2} \quad (25)$$

$$h_6 = \frac{1}{3}d + h_{dome,2} \quad (26)$$

$$h_7 = \frac{5}{4}d \quad (27)$$

$$h_9 = \frac{1}{4}d + 2h_{dome,1} \quad (28)$$

$$h_{11} = d \quad (29)$$

### C.1 Matrix of reaction forces

$A$  is a 33 by 33 matrix relating the different reactions while  $b$  represents the external loads applied, as previously mentioned at the barycenter of each component. The  $x$  column is composed by alternating iteratively the axial, transversal and torque reactions evaluated at the bottom of each component. Furthermore, the results accuracy is strictly related to the grid density.

In particular, the  $A$  is a sparse matrix where the diagonal element:

$$\begin{cases} A_{i,i} = 1 & \text{for } i = 2, 5, 8.. \\ A_{i,i} = -1 & \text{for } i \neq 2, 5, 8.. \end{cases} \quad (30)$$

while third lower sub diagonal:

$$\begin{cases} A_{i+3,i} = 1 & \text{for } i = 1, 4, 7.. \\ A_{i+3,i} = -1 & \text{for } i \neq 1, 4, 7.. \end{cases} \quad (31)$$

although for the fifth sub diagonal

$$\begin{cases} A_{i+4,i} = 1 & \text{for } i = 2, 5, 8.. \\ A_{i+4,i} = 0 & \text{for } i \neq 2, 5, 8.. \end{cases} \quad (32)$$

the resulting complete matrix is reported in the appendix. for what concerns the  $b$  columns:

$$\begin{cases} b_i = -m_i g_0 (n_1 + \sin(\gamma)) & \text{for } i = 1, 4, 7.. \\ b_j = -m_i g_0 (n_2 + \cos(\gamma)) & \text{for } i = 2, 5, 8.. \\ b_k = -m_i g_0 (n_2 + \cos(\gamma)) \frac{h_i}{2} & \text{for } i = 3, 6, 9.. \end{cases} \quad (33)$$

Furthermore, for the first  $b_i$  the drag should be added as an additional negative contributor, enhancing the beams compression. Where  $h_i$  is the length of the single component while  $n$  is the acceleration normalized with respect to the  $g_0$  and evaluated according the axial and transversal direction.

### C.2 Mechanical stresses

- Normal (Axial) Stress: in the form of compression, as a result of axial forces

$$\sigma_{normal} = \frac{F_{axial}}{A} \quad (34)$$

- Shear Stress: due to the shear force

$$\sigma_{shear} = \frac{F_{shear}}{A} \quad (35)$$

- Bending Stress: from the bending moment generated on the surface to counteract the effect of internal forces

$$\sigma_{bending} = \frac{M_{bending}R}{I} \quad (36)$$

- Lateral hoop stress: radial stress exerted by the pressurized fluid inside combined with hydrostatic pressure given the acceleration

$$\sigma_{hoop} = \frac{p_h R + \rho_{prop} g_0 n_x h R}{t} \quad (37)$$

- Axial stress of tank: axial stress exerted by the pressurized fluid inside combined with hydrostatic pressure given the acceleration

$$\sigma_{axial} = \frac{p_h R + \rho g_0 n_x h R}{2t} \quad (38)$$

Entire structure is treated to be consisting of only cylindrical shells. Therefore, area and area moment of inertia equations respectively are:

$$A = 2\pi R t \quad (39)$$

$$I = \pi R^3 t \quad (40)$$

Thickness of each component can be found via taking corresponding stresses into account and selection of an appropriate safety factor. Whichever of those stresses yielding maximum thickness is considered to be the critical stress and its resultant thickness shall be chosen. For internally unpressurized parts (i.e. void parts), critical buckling stress is:

$$\sigma_c = \sigma_{normal} + \sigma_{bending} = \left[ 9 \left( \frac{t}{R} \right)^{0.6} + 0.16 \left( \frac{R}{L} \right)^{1.3} \left( \frac{t}{R} \right)^{0.3} \right] \frac{Et}{R} \quad (41)$$

whereas for internally pressurized tanks, it is:

$$\sigma_c = \sigma_{normal} + \sigma_{bending} = \left\{ 9 \left( \frac{t}{R} \right)^{0.6} + 0.16 \left( \frac{R}{L} \right)^{1.3} \left( \frac{t}{R} \right)^{0.3} + \min \left[ 0.191 \frac{p}{E} \left( \frac{R}{t} \right)^2, 0.229 \right] \right\} \frac{Et}{R} \quad (42)$$

Additional term in Eq.(42) comes from the favoring effect of pressure inside the tank counteracting to compressive forces.

## D Appendix D:Aerodynamics

### D.1 Barrowman equation

Nose Cone Terms:

$$(C_N)_N = 2 \quad (43)$$

For Cone:

$$X_N = 0.666L_N \quad (44)$$

For Ogive:

$$X_N = 0.466L_N \quad (45)$$

Conical Transition Terms:

$$(C_N)_T = 2 \left[ \left( \frac{d_t}{d} \right)^2 - \left( \frac{d_t}{d} \right) \right] \Rightarrow X_T = X_P + \frac{L_T}{3} \left[ 1 + \left( 1 - \frac{d_t}{d_R} \right)^2 \right] \quad (46)$$

Fin Terms:

$$(C_N)_F = \left[ 1 + \frac{R}{S+R} \right] \left[ \frac{4N \left( \frac{S}{d} \right)^2}{1 + (1 + \left( \frac{2L_F}{C_R+C_T} \right)^2)^{0.5}} \right] \Rightarrow X_F = X_B + \frac{X_R(C_R + 2C_T)}{3(C_R + C_T)} + \frac{1}{6}(C_R + C_T) - \frac{(C_R \cdot C_T)}{(C_R + C_T)} \quad (47)$$

Finding the Center of Pressure:

$$(C_N)_R = (C_N)_N + (C_N)_T + (C_N)_F \quad (48)$$

$$\bar{X} = \frac{(C_N)_N X_N + (C_N)_T X_T + (C_N)_F X_F}{(C_N)_R} \quad (49)$$

## E Appendix E: Trajectory

### E.1 Evasive maneuver equations

$$R_t = \frac{v_{plane}^2}{g_0 \tan(\phi)} \quad (50)$$

$$\omega_t = \frac{v_{plane}}{R_t} \quad (51)$$

$$\begin{cases} x_{plane} = x_0 + v_{plane} \cos(\theta) \cdot t \\ y_{plane} = 0 \\ z_{plane} = y_0 + v_{plane} \sin(\theta) \cdot t \end{cases} \quad (52)$$

### E.2 Ascent trajectory equations

$$\begin{cases} \dot{V} = \frac{T \cos(\delta)}{M} - \frac{D}{M} - g \sin(\gamma) \\ \dot{\gamma} = \frac{T \sin(\delta)}{MV} + \frac{L}{MV} - \frac{g \cos(\gamma)}{V} + \frac{V}{r} \cos(\gamma) \\ \dot{r} = V \sin(\gamma) \\ \dot{\omega} = \frac{V \cos(\gamma)}{r} \\ \dot{m} = -\frac{T}{g_0 I_{sp}} \end{cases} \quad (53)$$

$$D = \frac{1}{2} \rho C_D A_{ref} v^2 \quad L = \frac{1}{2} \rho C_L A_{ref} v^2 \quad g = g_0 \left( \frac{R_\oplus}{R_\oplus + z} \right)^2 \quad (54)$$

### E.3 First stage re-entry

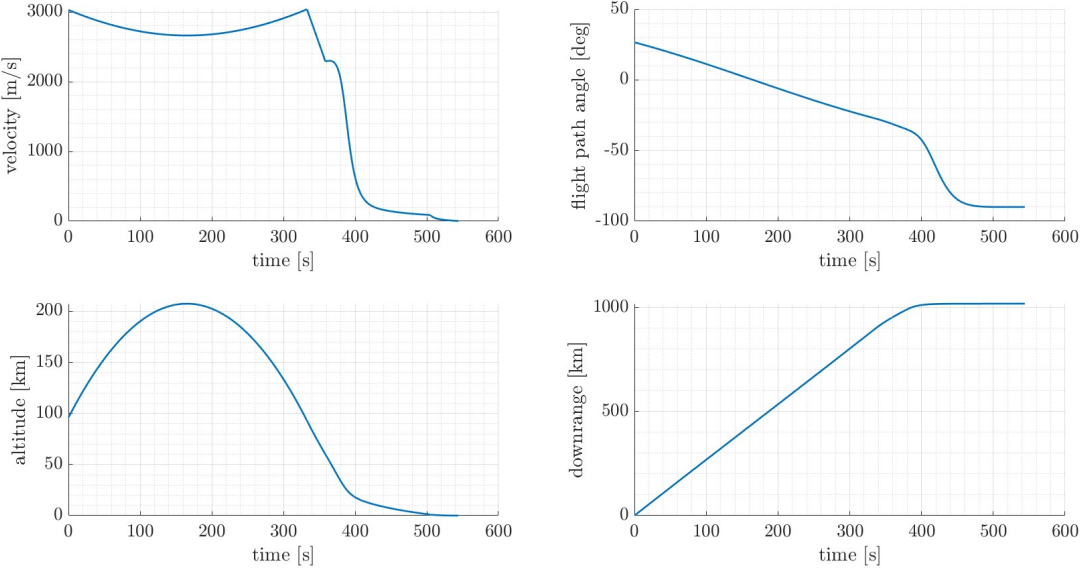


Figure 30: Trajectory parameters of Booster during re-entry

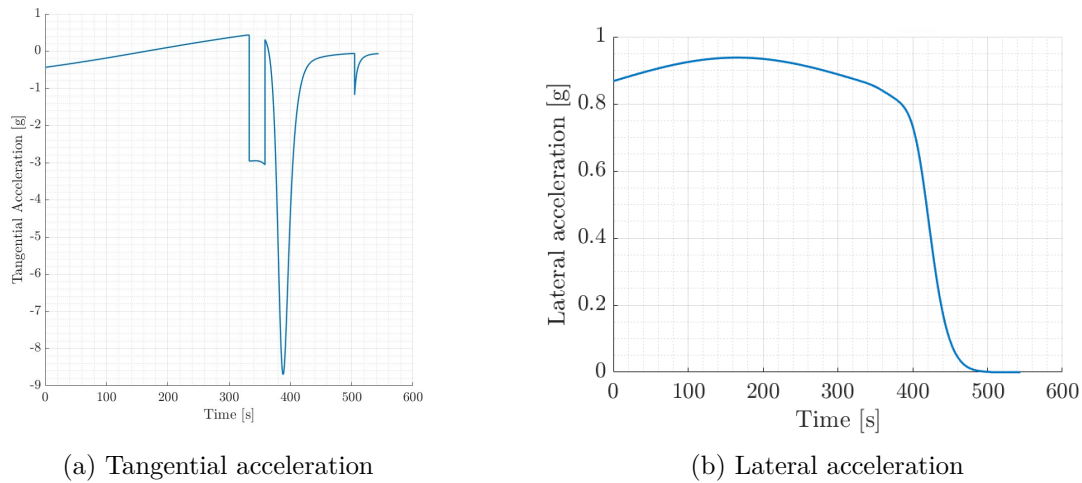


Figure 31: Re-entry booster acceleration components

Characteristics	Parachute system				
	Conical ribbon	Disk-gap-band	Modified ringsail	Cross	Ribless guide surface
Mach range(M)	0.1 < M < 2.0 up to M ~ 3.0 (WT tests)	M < 0.5 (WT tests) up to M ~ 2.6 (FF tests)	M < 0.5 up to M ~ 1.4 (FF tests)	Up to M ~ 1.64 (FF tests)	
Wind					
Tunnel(WT) free flight(FF)					
Drag	0.5–0.55	0.52–0.58	0.52–0.8	0.6–0.78	0.3–0.34
Coefficient(CD)					
Opening load factor	~ 1.05 – ~ 1.3	~ 1.3	~ 1.1	~ 1.2	~ 1.4
Average angle of oscillation	0 degrees – (±)3 degrees	(±)3 degrees – 6 degrees (WT tests)	~ (±)7 degrees	0 degrees – (±)3 degrees	0 degrees – (±)3 degrees
Canopy stability	Beginning of severe pulsation and ribbon flutter at M > 1.5	These parachutes were characterized by partial collapse and fluctuations of the canopy immediately after the first inflation peak at Mach numbers M > 1.4. The partial collapse was most severe for the disk-gap-band configuration and least severe for the modified ringsail system Stable for M < 1.4		Never stable in 1.1 < M < 1.64	No data available

Figure 32: Parachute limits<sup>[30]</sup>

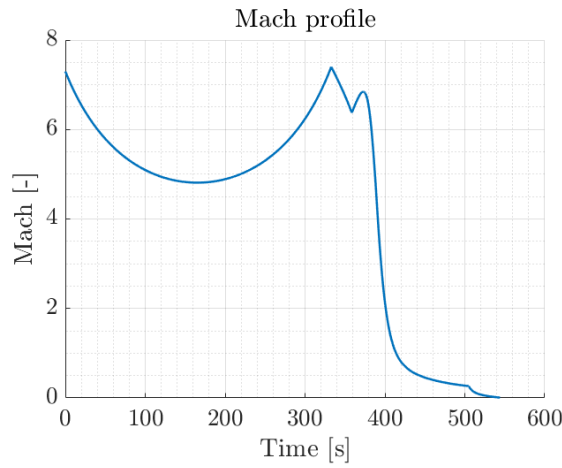


Figure 33: First stage Mach profile during re-entry

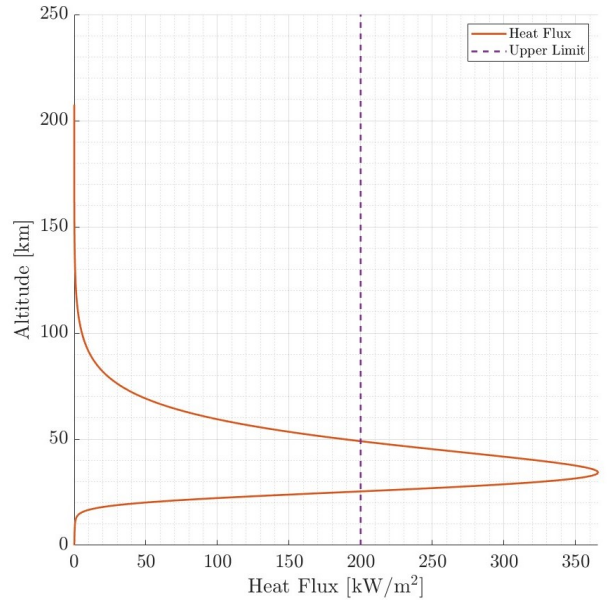


Figure 34: Heat flux profile of first stage during natural re-entry

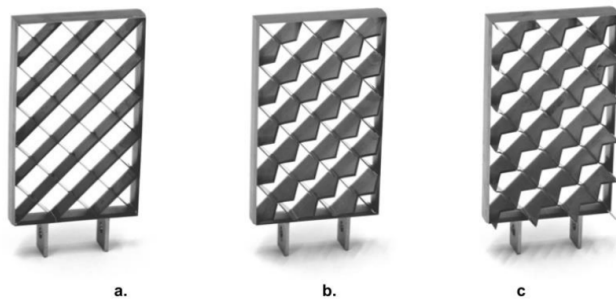


Figure 35: Grid Fins Configurations of Unswept (a), Locally Swept (b)(c)<sup>[38]</sup>

#### E.4 Second stage re-entry

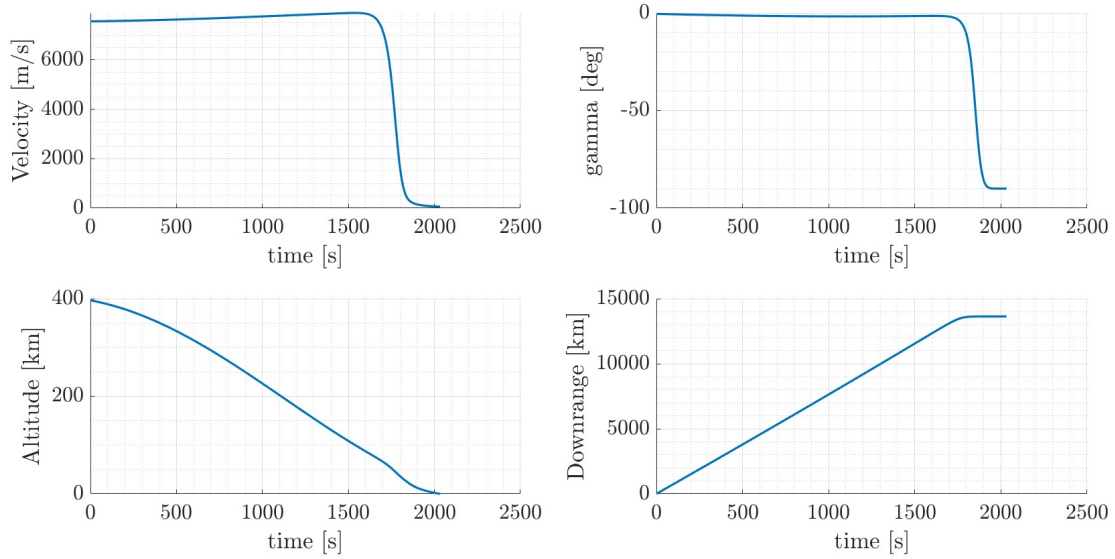


Figure 36: Stage 2 re-entry parameters

## E.5 SSO Orbit

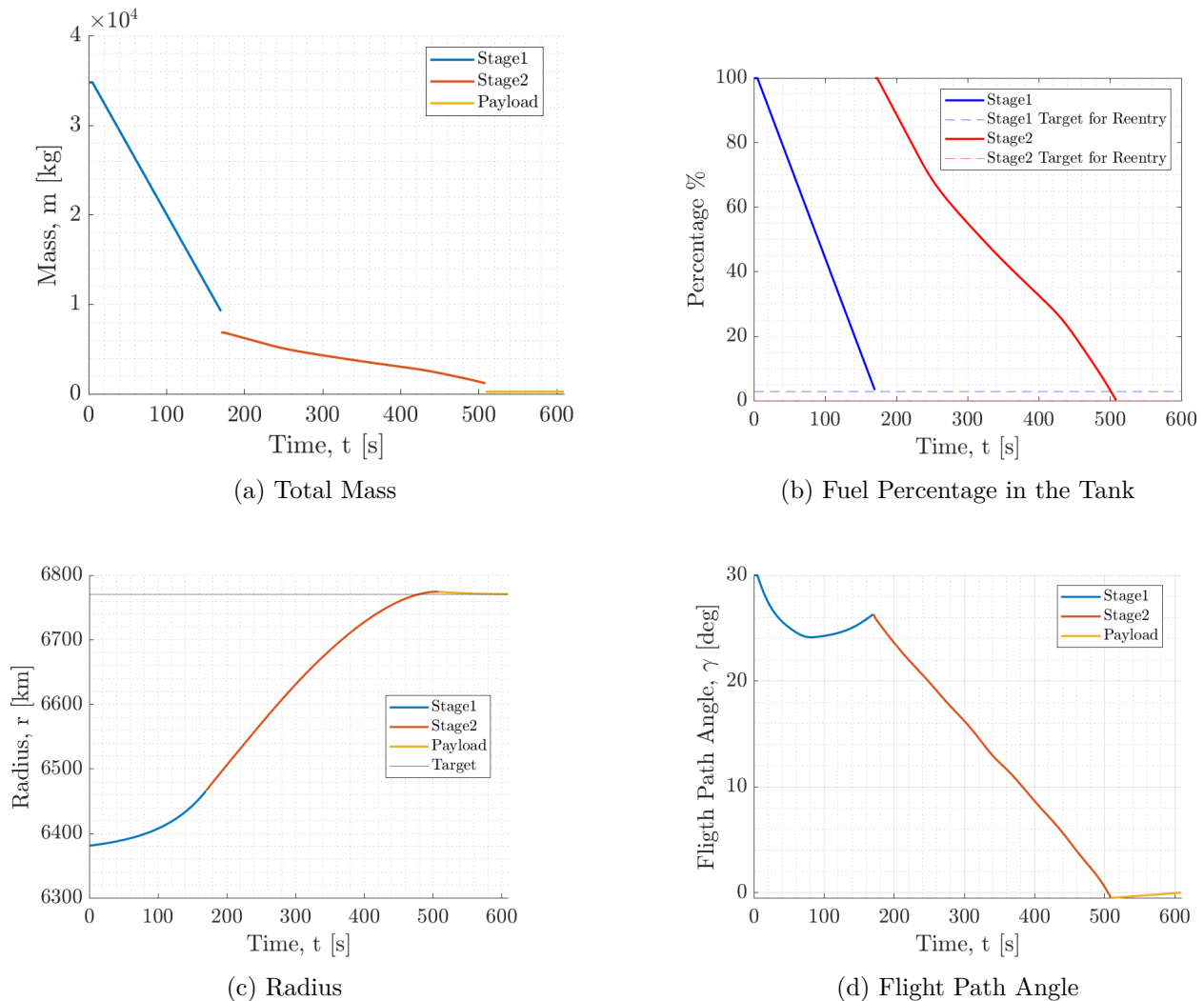
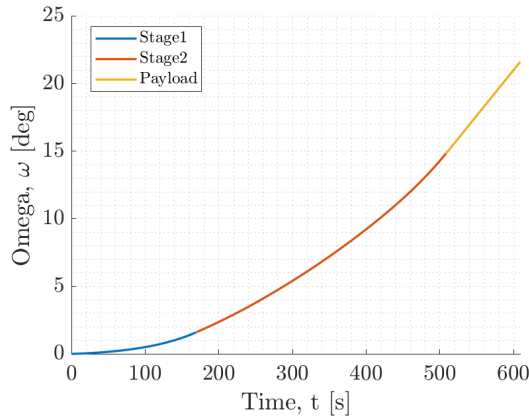
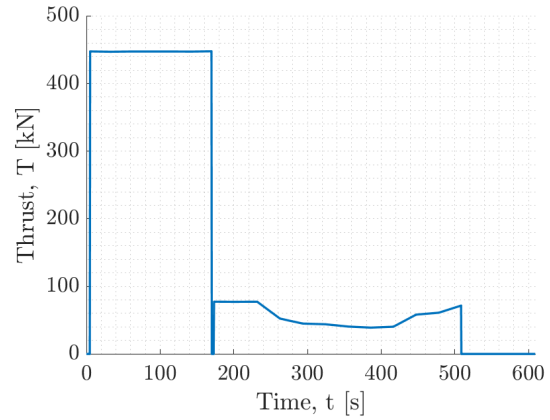


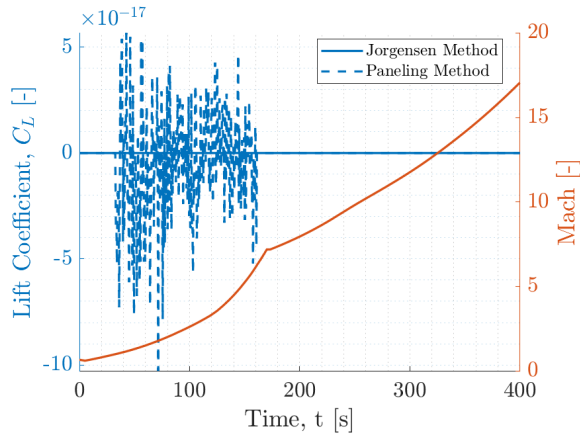
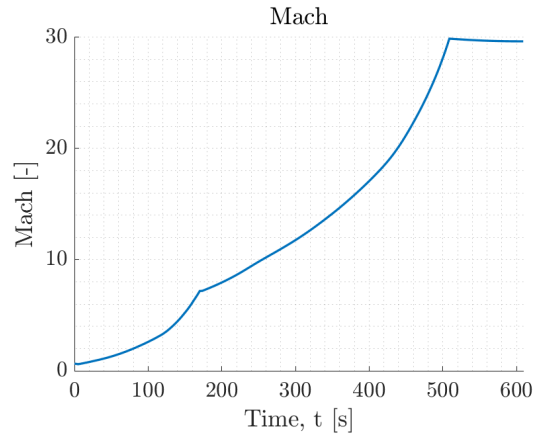
Figure 37: SSO Trajectory Results



(a) Angular Velocity of Radius

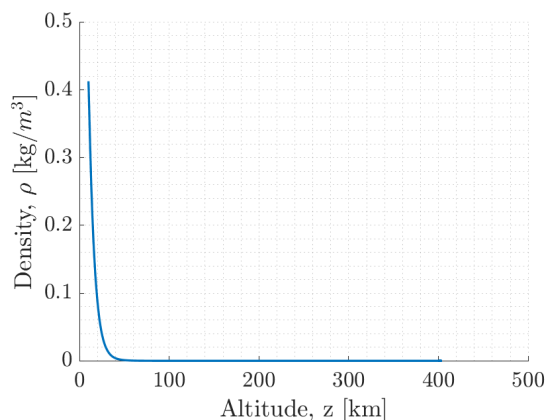


(b) Thrust Profile

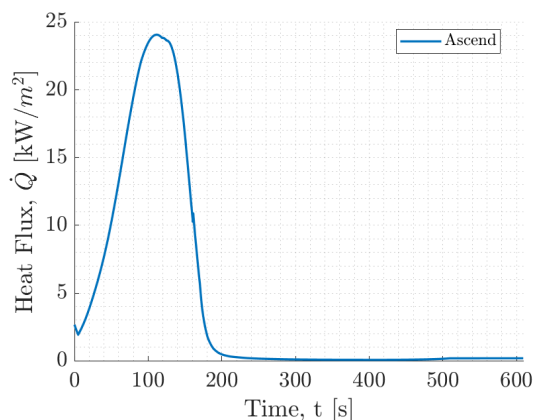
(c) Lift Coefficient  $C_l$ 

(d) Mach Number

Figure 38: Result of the Optimization Process SSO



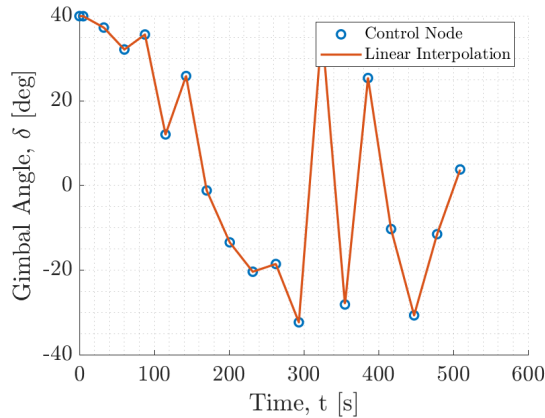
(a) Atmospheric Density



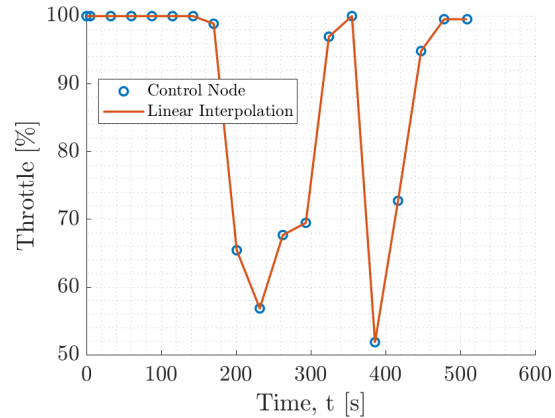
(b) Thermal Load During Ascent

Figure 39: Result of the Optimization Process SSO

## E.6 Equatorial Orbit

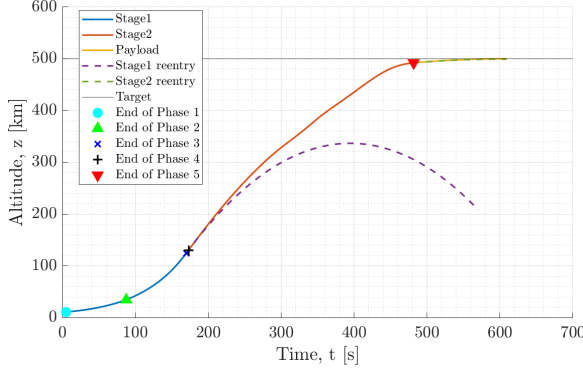


(a) Gimbal Angle

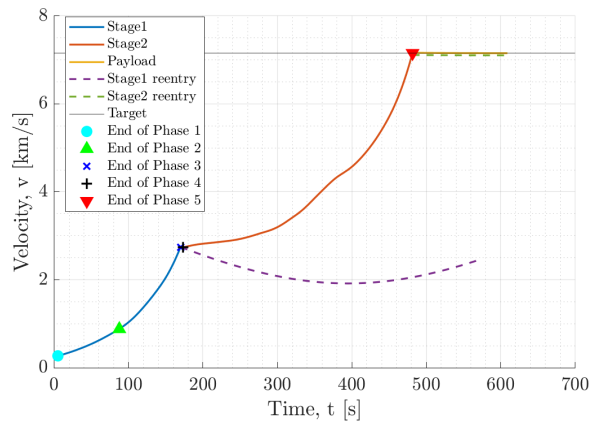


(b) Throttle of the Engine

Figure 40: Comparison of the Control Variable Equatorial Orbit

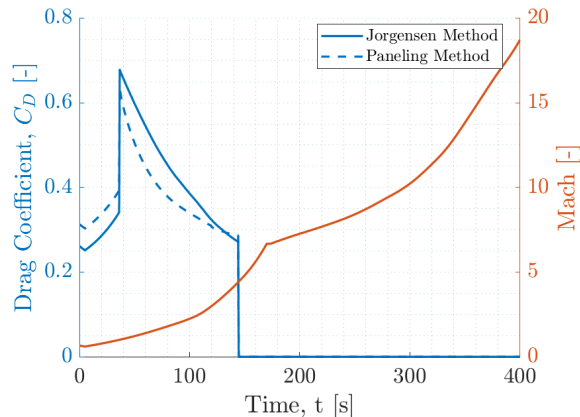
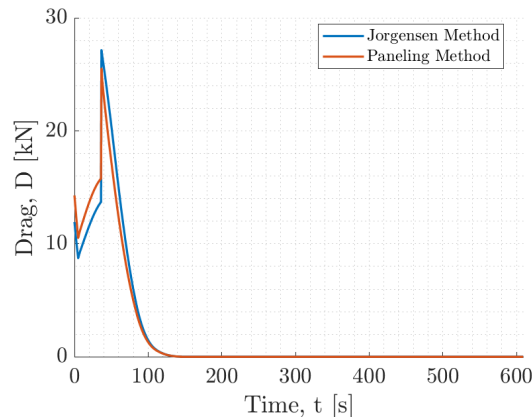


(a) Altitude



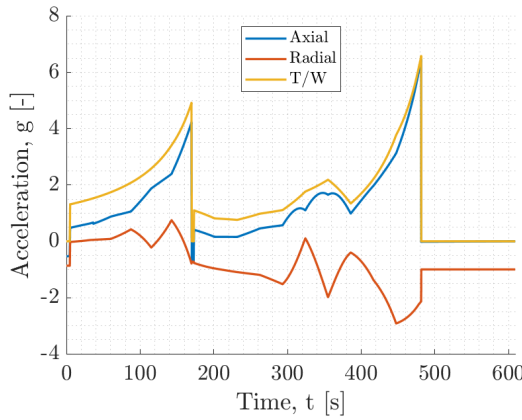
(b) Velocity

Figure 41: Result of the optimization process Equatorial Orbit

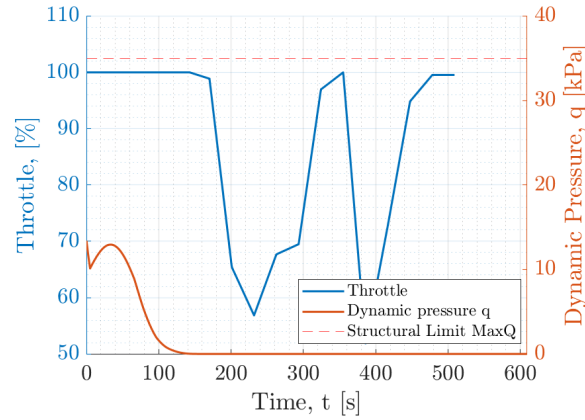
(a)  $C_D$  and Mach Number over time

(b) Drag during the Trajectory

Figure 42: Comparison of Aerodynamic Models Equatorial Orbit

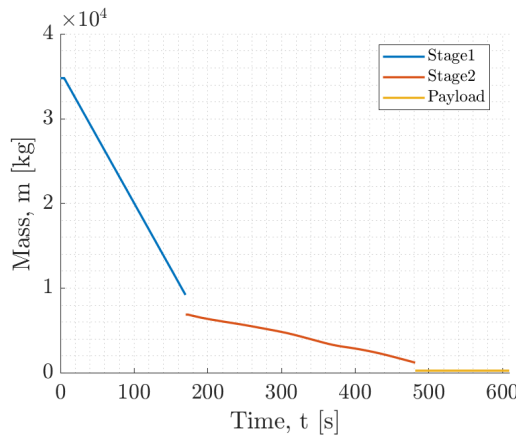


(a) T/W, Radial and Axial Acceleration

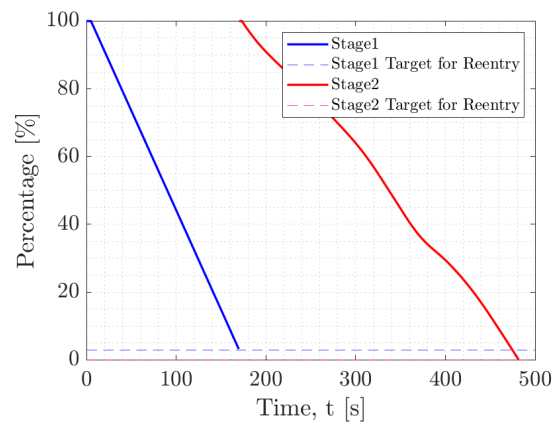


(b) MaxQ and Throttling

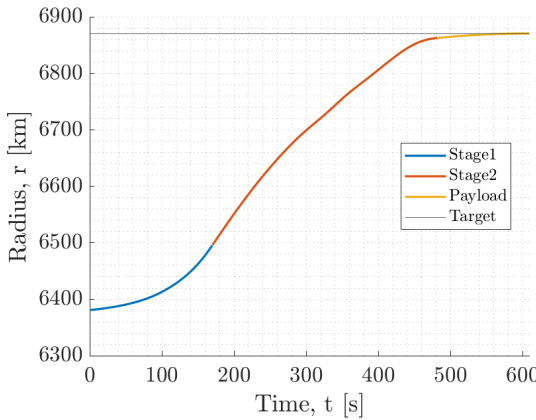
Figure 43: Structure Results Equatorial Orbit



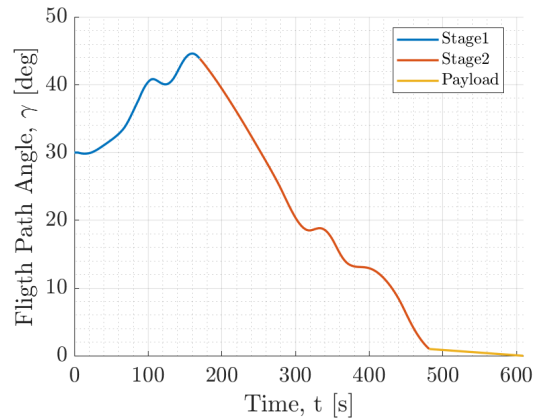
(a) Total Mass



(b) Fuel Percentage in the Tank

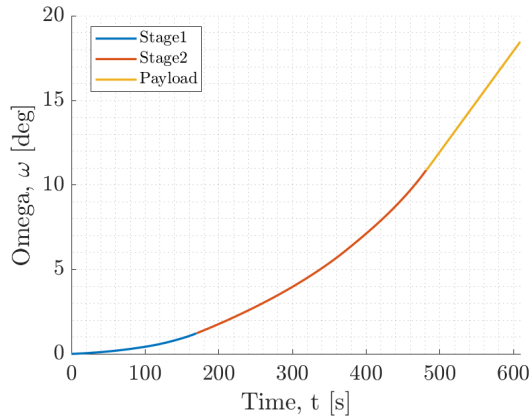


(c) Radius

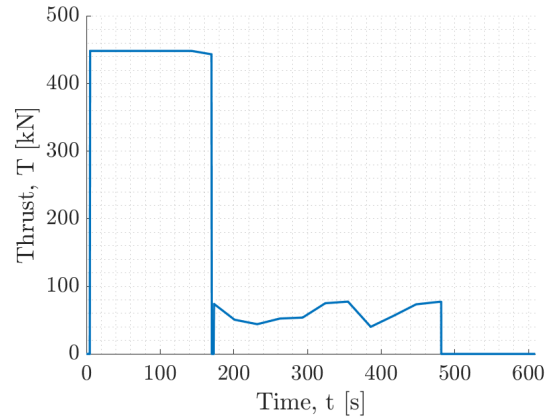


(d) Flight Path Angle

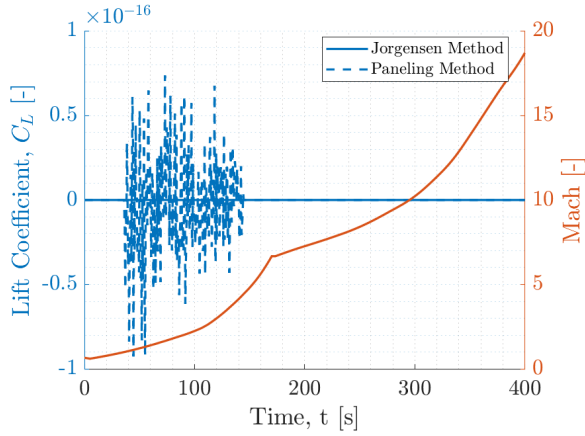
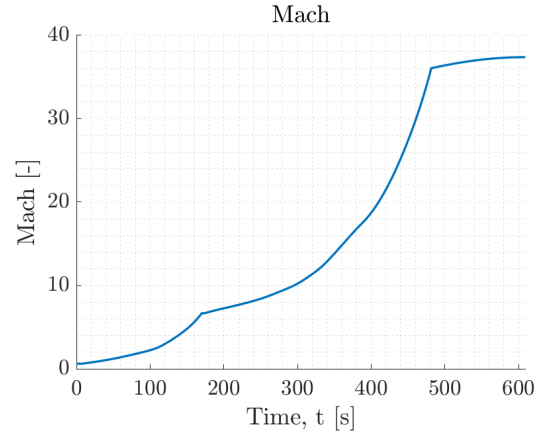
Figure 44: Result of the Optimization of Equatorial Orbit



(a) Angular Velocity of Radius

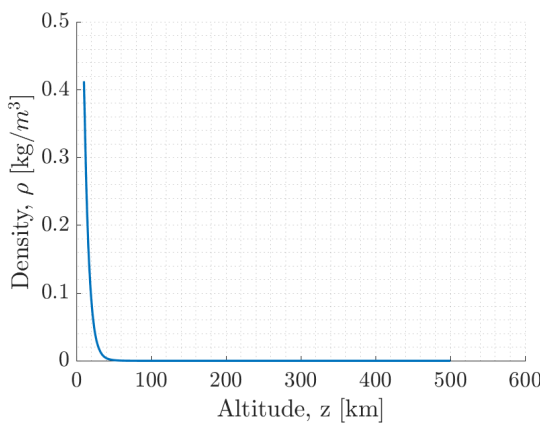


(b) Thrust Profile

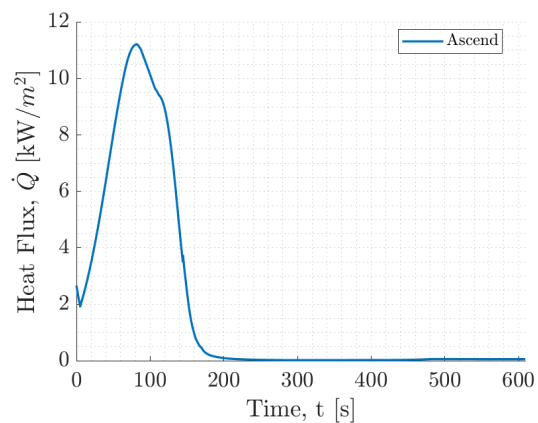
(c) Lift Coefficient  $C_l$ 

(d) Mach Number

Figure 45: Result of the Optimization of Equatorial Orbit



(a) Atmospheric Density



(b) Thermal Load During Ascent

Figure 46: Result of the Optimization Process Equatorial Orbital

## F Appendix F: Monte Carlo Analysis

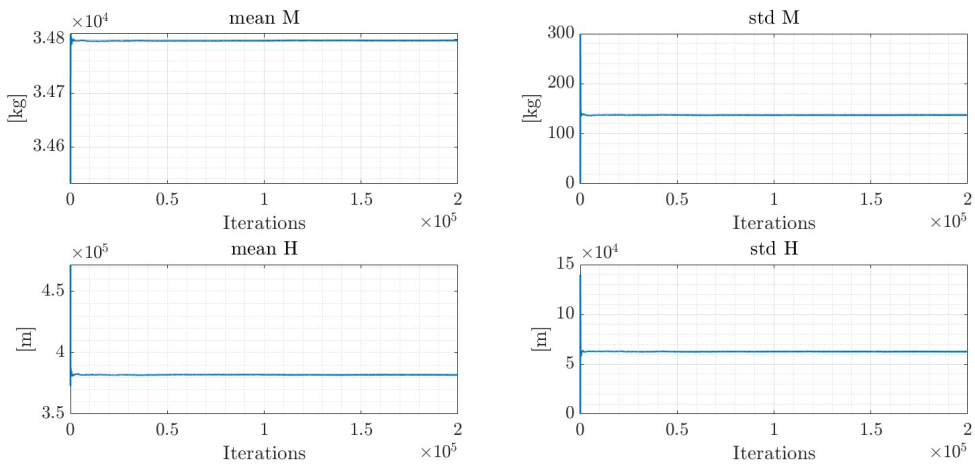


Figure 47: Evolution of mean and standard deviation

## G Appendix G: Costs analysis and Return On Investment (ROI)

The estimation begins with a power curve relationship, which establishes a correlation between the masses of the launcher's main components and their respective costs:

$$C = a \cdot M^b \quad (55)$$

where  $C$  and  $M$  are the cost and the mass of the component respectively and  $a$  and  $b$  are coefficients derived from historical data. The cost  $C$ , later on referred to as  $FM1$  (First Flight Model), is the basis for estimating the development and manufacturing costs. Development costs include the processes of design, qualification, and testing for each launcher component. These processes require the construction of several hardware models, specifically: Design, Engineering, Protoflight and Flight Models ( $DM, EM, PFM, FM$ ). An exception is made for the engines, which only require the PFM and FM, as they are purchased off-the-shelf and undergo only minor modifications, such as adjustments to the nozzle exit area. The ensemble of these models forms the System Test Hardware ( $STH$ ), that combined with  $FM1$  results in Manufacturing, Assembly, Integration and Test ( $MAIT$ ) costs. Instead,  $FM1$  cost, combined with the Design and Development ( $DD$ ) factors, is used to estimate the Engineering ( $ENG$ ) costs. The total development cost is thus computed as:

$$DEV = (1 + S_m^{-1}(M/PA_p\% + I\&T\%_p)) \cdot \sum_{i=1}^n c_p \{ [FM1 \cdot DD \cdot (S_m^{-1} \cdot M/PA_p\%)] + [FM1 \cdot STH \cdot L_d \cdot \#HW] \} \quad (56)$$

where  $S_m$  is a scaling factor accounting for the reduced management effort, due to having only one subcontractor for the engines and for the same reason the profit retention factor  $c_p$  is introduced,  $M/PA_p\%$  and  $I\&T\%_p$  are coefficients representing the management and integration and testing costs,  $L_d$  is a learning factor associated with production efficiency gains during development and  $\#HW$  is the number of units produced for the same element. The total development cost is amortized over  $N_a = 100$  launches to calculate the  $CpF$ . This ensures a proportional distribution of the development expense across the expected number of launches.

The next step involves computing the manufacturing costs. These costs are estimated under the assumption that the components of the first stage are manufactured every 5 launches. Additionally, a production cost improvement is applied, following the same principles as the one used in the development phase ( $L_d$ ). The total manufacturing cost is then calculated as:

$$MAN = (1 + S_m^{-1}(M/PA_p\% + I\&T\%_p)) \cdot \sum_{i=1}^n c_p [FM1 \cdot n^b \cdot (1 + M/PA_p\%)] \quad (57)$$

$n^b$  is the aforementioned production cost improvement factor, where  $n$  represents the  $n$ -th unit produced and  $b$  is a function of the learning factor  $p$ , calculated as  $b = \frac{\ln(p)}{\ln(2)}$ .

The final calculation involves estimating the operations costs ( $OPS$ ), which encompass the following components: Ground Operations ( $GO$ ), Propellant Cost ( $PC$ ), Flight and Mission Operations ( $FMO$ ), Transportation Costs ( $TC$ ), Fees and Insurance Costs ( $FIC$ ), Carrier Costs ( $CC$ ) and Indirect Operating Costs ( $IOC$ ).

The final  $CpF$  is calculated as the sum of the development, manufacturing, and operations costs, with additional contributions for: recovery costs ( $C_{REC}$ ), representing 50% of the operations costs to account for retrieving the first stage and the refurbishing costs ( $C_{REF}$ ), estimated at 30% of the manufacturing costs for reconditioning the first stage for reuse:

$$CpF = \frac{DEV}{N_a} + MAN + OPS + C_{REC} + C_{REF} \quad (58)$$

Assuming a profit margin of 8% over the  $CpF$ , the Price per Flight ( $PpF$ ) is determined. To this, an additional 5% of  $CpF$  is added to cover payload insurance, resulting in the final User Price ( $UP$ ).

After completing the cost analysis, the Return on Investment (ROI) is computed. The initial value of  $CpF$  is considered as the total investment made by the customer for the project. The computation

is performed iteratively over 20 launches ( $n$ ), under the following assumptions: a portion of the User Price ( $UP$ ) is allocated to fund the subsequent launch and the remaining amount is distributed between the investor and the company in the ratio of  $\frac{2}{3}$  and  $\frac{1}{3}$  respectively. The ROI is then computed using the sum of the dividends given to the investor across all launches:

---

**Algorithm 1:** ROI computation Algorithm

---

```

1 for  $i \rightarrow 1$  to  $n$  do
2    $profit(i - 1) = UP(i - 1) - CpF(i);$ 
3    $investor(i - 1) = \frac{2}{3} \cdot profit(i - 1);$ 
4    $company(i - 1) = \frac{1}{3} \cdot profit(i - 1);$ 
5    $ROI(i - 1) = \frac{\sum investor - CpF(1)}{CpF(1)} \cdot 100;$ 
6 end

```

---

## Authorship declaration

- **Bianco Samuele:** LV loads and stress analysis, thicknesses computation. Paneling and Jørgensen method.
- **Campanino Mattia:** System engineer, Cost Analysis and ROI computation
- **Cutino Sveva:** Simulation of Evasive Maneuver, simulation of Re-entry. Literature analysis for stage 2
- **D'Annunzio Valentina:** Mission Analysis ( $\Delta v$  budget), Propulsion subsystem, Cost Analysis and ROI computation
- **D'Antonio Antonio:** Simulation of Evasive Maneuver, simulation of Re-entry. Literature analysis of thermal environment of stage 1 during re-entry.
- **Dell'Aera Nicola:** Structural verification of the airplane, Monte Carlo simulation, panel method.
- **de Pinto Alessio:** Masses computation, MERs model, staging, sizes computation apart from fairing literature analysis
- **Orsenigo Samuele:** Mission Analysis and Trajectory Optimization
- **Santoro Emanuele:** Propulsion subsystem and Functional decomposition
- **Varli Arda:** Payload fairing sizing, structural matrix formation